

ABSTRACT

Late Quaternary Sedimentary Architecture and Depositional History of the Monahans
Dune Field, Winkler County, TX

Connor J. Mayhack, M.S.

Mentor: Steven L. Forman, Ph.D.

The Monahans dune field is a Quaternary eolian system on the Southern High Plains in west Texas. Previous work characterizing the Monahans is limited by the depth and spatial coverage of stratigraphic analyses. This study presents the initial results of an ongoing study of the dune system facilitated by the collection and analysis of 81 sonic boreholes (>40 m) and 18 Geoprobe direct push cores (5-19 m). Three-dimensional modeling of these data, and exploratory passive seismic observations reveals a complex depositional record of eolian and palustrine deposition, and pedogenesis. This study analyzes the depositional sequence, geometry and chronology of Blackwater Draw Formation (BWD) and coeval lacustrine sequence. Sonic boring infill logs and geophysical exploration records were used to define the basal depositional surface. The eolian sands and in fill across a northwest to southeast slope thinning eastward to an escarpment and subsurface depressions which are not reflected in the current topography.

The chronology of the near-surface stratigraphy was derived from Optically Stimulated Luminescence (OSL) and Thermal Transfer (TT-OSL) Single Aliquot Regeneration (SAR) protocols on quartz grains from in-tact sediment cores. The stratigraphy and chronology of quartz grains from these cores document thirteen eolian deposition phases (EDPs). These phases document a recurring cycle of eolian activity, stabilization and pedogenesis, and erosion. The results of this study provide new insight into sedimentary structures, processes, and depositional history within the Monahans dune system, and relationship with climate variability in the late Quaternary Southern High Plains.

Late Quaternary Sedimentary Architecture and Depositional History of the Monahans Dune Field,
Winkler County, TX

by

Connor Mayhack, B.S.

A Thesis

Approved by the Department of Geosciences

Joseph Yelderman, Ph.D., Chairperson

Submitted to the Graduate Faculty of
Baylor University in Partial Fulfillment of the
Requirements for the Degree
of
Master of Science

Approved by the Thesis Committee

Steven L. Forman, Ph.D., Chairperson

Daniel Peppe, Ph.D.

Joseph Ferraro, Ph.D.

Accepted by the Graduate School

August 2021

J. Larry Lyon, Ph.D., Dean

Copyright © 2021 by Connor J. Mayhack

All rights reserved

TABLE OF CONTENTS

LIST OF FIGURES	vii
LIST OF TABLES	ix
ACKNOWLEDGMENTS	x
CHAPTER ONE	1
Introduction.....	1
Geologic Setting.....	4
Scientific Objectives and Hypotheses.....	7
CHAPTER TWO	8
Methods.....	8
Sedimentology, Pedology, and Stratigraphy.....	8
Optically stimulated luminescence dating	9
Three-dimensional (3-D) Stratigraphic Modeling of the Monahans's.....	13
CHAPTER THREE	15
Results.....	15
Pedosedimentary facies for Monahans eolian sediments.....	15
Logs of Sonic Borings	17
Geoprobe Sediment Cores	18
Field Area A.....	24
Field Area B	26
Field Area C.....	28
3D Modeling of Monahans subsurface geometry	29
CHAPTER FOUR.....	34
Discussion.....	34
Conclusions.....	39
APPENDIX.....	41

Figures and Tables.....	44
References.....	49

LIST OF FIGURES

FIGURE 1. A) Position of the Monahans Dune field (Insert) relative to the Southern Great Plains (grey) and mapped surficial eolian deposits (brown) after Holiday et al, 1995. B) The extent of 3D modeling (white) and position of Sonic borings (red) and Geoprobe cores (yellow).	1
FIGURE 2. A) trajectory of N. Hemisphere storm tracks and warm subtropical air during Warmer interstadial conditions relative to the Monahans (yellow). B) Southern excursion of these synoptic features during cold stadial conditions and greater Laurentide extent. Schmidt and Hertzberg, (2011)	2
FIGURE 3. Locations of Sonic Boreholes collected in the Monahans dune field. Borehole locations marked in blue.....	17
FIGURE 4. Log of cuttings collected from Sonic Borehole AT2-17-1. The log describes color, texture, and moisture of sediments with recorded depths of diagnostic changes	18
FIGURE 5. Stratigraphy of geoprobe cores collected from field area A with core locations inset.....	25
FIGURE 6. Stratigraphy of geoprobe cores collected from field area B with core locations inset.....	27
FIGURE 7. Stratigraphy of geoprobe cores and surface exposure from field area C with locations inset.....	28
FIGURE 8. Extent of 3D modeling with data sources: sonic borings (red), geoprobe cores (yellow), geophysical survey lines (blue)	30
FIGURE 9. Elevation model of the basal alluvium, in which the Blackwater Draw rests on with color graded contours in meters above mean sea level.....	30
FIGURE 10. Schematic cross section ABB' of the Monahans dune field. The modeled pluvial lake and carbonate soil deposits represent a minimum extent.....	31
FIGURE 11. Cross section A-A' of Monahans subsurface deposition presented with 20x vertical exaggeration. Location of cross section shown in Fig. 8	32

FIGURE 12. Composite chronology of the Monahans Dune Field. Depicted are eolian depositional phases (numbered 1-13), pluvial deposition (blue), primary facies encountered in geoprobe cores, and luminescence ages of eolian deposits..... 36

FIGURE 13. Distribution of Monahans Luminescence Ages. This figure plots both a probability density function (PDF) of all ages collected >1ka (blue) as well as the 11 populations (black line with associated errors in grey) identified by a finite mixture model (FMM). Each of the ages (n=57) is represented by a grey hash and grey dot with associated errors... 38

FIGURE A.1. Stratigraphy of geoprobe core MON17-1..... 42

FIGURE A.2. Stratigraphy of geoprobe core MON17-2..... 42

FIGURE A.3. Stratigraphy of geoprobe core MON17-4..... 43

FIGURE A.4. Stratigraphy of geoprobe core MON17-5..... 43

FIGURE A.5. Stratigraphy of geoprobe core MON17-6..... 44

FIGURE A.6. Stratigraphy of geoprobe core MON17-7..... 44

FIGURE A.7. Stratigraphy of geoprobe core MON17-8..... 45

FIGURE A.8. Stratigraphy of geoprobe core MON18-12..... 45

FIGURE A.9. Stratigraphy of geoprobe core MON18-13..... 46

FIGURE A.10. Stratigraphy of geoprobe core MON18-14.....46

FIGURE A.11. Stratigraphy of geoprobe core MON18-17..... 47

FIGURE A.12. Stratigraphy of geoprobe core MON19-30..... 47

FIGURE A.13. Stratigraphy of geoprobe core MON19-31..... 48

LIST OF TABLES

TABLE 1. Pedo-sedimentary facies of Monahans cores.....	16
TABLE 2. Optically stimulated luminescence (OSL) and Thermal Transfer OSL (TT-OSL) ages on quartz grains from eolian sands, Monahan's dune field, west Texas.....	20
TABLE 3. Table 3. Finite mixture model components with associated errors of Monahans dune field luminescence ages. Those defined by less than five ages are listed in red.....	38

ACKNOWLEDGMENTS

First, I would like to thank Dr. Steve Forman for chairing my thesis committee and for your mentorship, guidance, and perennial patience. Your instruction and example have had an indelible impact on my academic career and life. I would also like to thank Dr. Dan Peppe for serving as one of my thesis committee members, your service as a conscientious graduate program director. Dr. Joseph Ferraro, thank you for serving as one of my thesis committee members and the constructive feedback on my proposal which has helped shape this thesis.

Dr. Logan Weist – Thank you for your instruction in both field and lab settings which have shaped my approach to stratigraphy and sedimentology, and your tireless work in the field.

Thank you, Liliana Marin, for your mentorship, and instruction in Luminescence dating methods.

Thank you, Victoria Tew-Todd, for your assistance in the field, the lab, and your friendship

Thank you, Peng Liang for your assistance in the field and contribution of the LDAC software.

Thank you, Atlas Sands and especially Griffin Money for the generous access and support which has made this work possible.

CHAPTER ONE

Introduction

The Monahans Dune Field, Winkler County, Texas is one of numerous Quaternary eolian systems on the Great Plains (Fig. 1). Many of these eolian systems have persisted on the landscape for tens of thousands, if not millions of years (e.g. Forman et al., 2001, Rich and Stokes 2011, Halfen and Johnson, 2013); reflecting landscape-scale eolian and ecosystem processes (Schlesinger et al., 1990, Bolles and Forman, 2018). The activity of these North American dune fields is modulated by the wind velocity, sediment availability and source mediated by vegetation cover (Turnbull et al., 2010, Bolles and Forman, 2018).

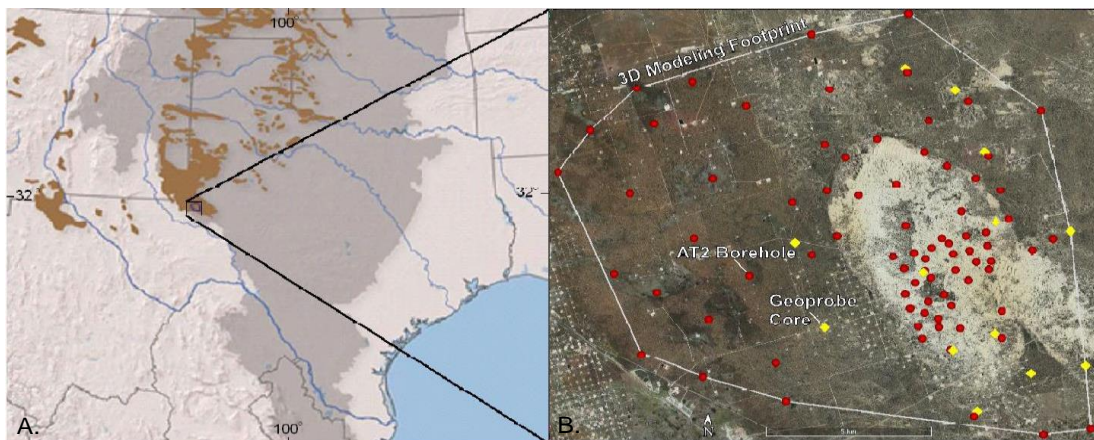


Figure 1. A) Position of the Monahans Dune field (Insert) relative to the Southern Great Plains (grey) and mapped surficial eolian deposits (brown) after Holiday et al, 1995. B) The extent of 3D modeling (white) and position of Sonic borings (red) and Geoprobe cores (yellow).

Thus, an emerging paradigm has established a corollary relationship between the drivers of climate in the Southern High Plains (SHP), the latitudinal and elevational extent of the Laurentide Ice

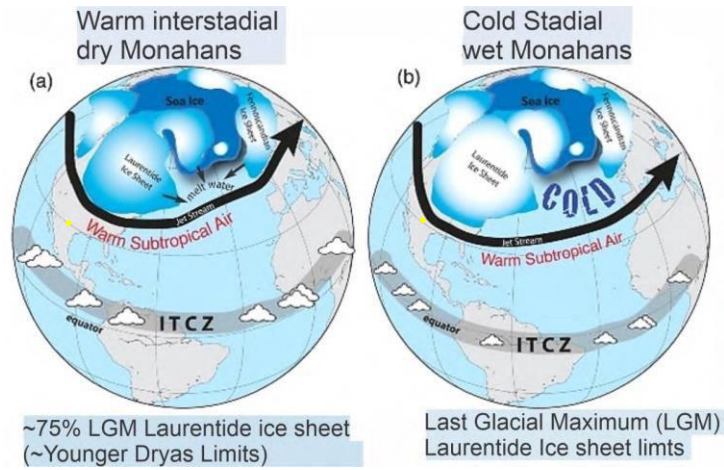


Figure 2. a) trajectory of N. Hemisphere storm tracks and warm subtropical air during Warmer interstadial conditions relative to the Monahans (yellow). b) Southern excursion of these synoptic features during cold stadal conditions and greater Laurentide extent. Schmidt and Hertzberg, (2011)

Sheet, synoptic scale atmospheric oscillations, and the associated North American Monsoon (Fig. 2) (Forman et al., 2001, Halfen and Johnson, 2013, Donat et al., 2015). The stratigraphic record of eolian deposition in the Southern Great Plains may reflect wetter periods during glacials and stadials and considerably drier times with interglacials and interstadials in the late Quaternary. This study evaluates the sedimentary architecture of Monahans Dune Field using data developed from sonic borings, Geoprobe cores, and three-dimensional stratigraphic modeling. This analysis provides new insights on the geometry of the Monahans eolian depositional basin and the timing and pace of eolian deposition and pedogenesis in relation to the ancestral Pecos River.

Modern drought variability on the SHP is driven by ENSO. This synoptic oscillation drives SHP drought as upwelling and cTolder SSTs in the eastern tropical pacific induce high pressure systems during positive La Niña phases (Cook et al.,

2011, Ternberth and Hurrell 1994, Donat et al., 2015). Cooling in tropical waters reduce meridional temperature and pressure gradients and result in a poleward contraction of the westerly jets (Cook et al., 2011). The meridional extent of the jet stream driven by the expansion and contraction of the Hadley Cell shifts the mid-latitude storm tracks (Schubert et al., 2004, Cook et al., 2009). Such changes to the temperature and pressure fields driving North American circulation suppress the major transport of moisture from the Gulf of Mexico into central and southern North America (Donat et al., 2015). This moisture is associated with the Great Plains Low Level Jet (GPLLJ), a local summer wind system which transports moisture into the North American continent from the Gulf of Mexico (Donat et al., 2015). The suppression of this local system by synoptic circulation results in the southerly spring flow of the GPLLJ being sideswept northeastward along the Atlantic margin (Donat et al., 2015). This change results in spring and early summer winds transporting dry continental air over the SHP (Donat et al., 2015).

Climate during the late Pleistocene to Holocene North American atmosphere was modulated intermittently by the Laurentide Ice Sheet. This ice sheet impacted global heat balance and atmospheric dynamics in several ways. Increased meltwater events reduced thermohaline circulation and altered meridional heat transport (Jackson, 2000) reducing North Atlantic SSTs which have been observed and modeled to have a major influence on modern drought conditions in the Great Plains (Donat et al., 2015, Schubert et al., 2004, Cook et al., 2011). In addition, the ice sheet elevation (Jackson, 2000) and position (Romanova et al., 2006) anchored a tropospheric stationary wave due to the orographic and temperature gradient impacts.

The result is that as the planet transitions between glacial or stadial and interglacial to interstadial conditions, the extent and height of the LIS modulates the position of mean storm tracks across the Great Plains (e.g. Holiday, 1989, Gustavson and Holiday, 1999, Holiday, 2001, Rich and Stokes, 2011). During warm Interstadials, the coalescence of Northern hemisphere jet streams contracts poleward towards the margin of the ice sheet resulting in warm subtropical air from the continent being transported across the SHP. Alternatively, during colder Stadial conditions, the stationary wave produced by the LIS deflects the jet stream and associated storm tracks further South, resulting in pluvial conditions in the SHP. This study aspires to expand our understanding of late Quaternary paleoclimate in the SHP as by observation of its expression in the eolian depositional and pedologic history of the Monahans Dunes.

Geologic Setting

The modern sand sheet and dune field observed at the surface in the Monahans is deposited over the Blackwater Draw Formation (BWD). The Blackwater Draw contains eolian, fluvial, colluvial sediments with prominent carbonate-rich buried soils which occurs across much of the SHP (Gustavson and Holiday, 1999, Holiday, 2001). Six major paleosols (Carbonate stage II-IV) are identified near the type section with as many as fourteen soils and paleosols recorded in sediment cores (Gustavson and Holiday, 1999, Hovorka, 1995). The base of the BWD Formation is inferred to be Plio-Pleistocene, ca. 1.6 Ma old, based on the occurrence of the Ma Guaje Ash in a lower stratigraphic position (Holliday 1989).

Luminescence and radiocarbon ages on quartz grains constrain the upper eolian deposits to span the late Pleistocene, ca. < 200 ka and terminate at the Pleistocene to Holocene boundary at ca. 12 ka (Holliday et al. 2008, Rich and Stokes, 2011; Rich 2013). Late Pleistocene strata in the Monahans Dune Field is characterized by quartz-dominated eolian sands intercalated with paleosols that in places have been truncated by erosion. Paleosols often show well developed calcic and argillic horizons indicative of prolonged stability (> 5 ka) and more mesic conditions (Gustavson and Holliday 1999).

Another key to understanding the Monahans eolian system is the context provided by proximal sand sheet deposits in New Mexico and northern Mexico. These sequences reveal multiple distinct reactivation periods in the past 100 ka (e.g. Hall et al. 2010, Hall and Goble 2015, Rich, 2013). For example, the Mescalero sand sheet deposit extends west of the caprock escarpment to the northeast edge of the Chihuahuan Desert. This sand sheet is composed of two depositional episodes, overlying Mescalero paleosol with carbonate stage II – III morphologies (Hall and Goble 2006). This paleosol formed prior to 100 ka on the eroded surface of Permian and Triassic Red beds and the Middle Pleistocene Gatuña Formation (Hall and Goble 2006, Hall and Goble 2008). OSL ages on quartz grains from the overlying eolian sands indicate deposition between ca. 90 and 70 ka, and 9 and 5 ka ago (Hall and Goble, 2008). Further to the east, the Bolson sand sheet also exhibits two phases of deposition, constrained by OSL ages between ca. 44.5 ka and 22.2, and 22.2 and 5.2 ka (Hall et al. 2010). The earliest episode is coincident with a transition from subaerial to paludal-lacustrine conditions in nearby Lake Otero, NM at 47 ka (Hall et

al. 2010, Allen et al. 2009). Deflation across the SHP has also resulted in smaller scale lunette features with periodic deposition 25-15 ka, and 8-5 ka (Holliday 19997, Holliday et al. 2008).

Pluvial lakes Otero and Estancia in northern New Mexico record a series of high stands in the ca. 22 to 15 ka, the onset followed by a pronounced fall in lake level at ca. 18.1-17 ka (Broecker et al. 2009, Menking et al. 2018). Lake Otero experienced its final highstand ca. 16.9 ka (Menking et al. 2018). Initial desiccation and deflation and of both basins occurred between 12 and 11.3 ka (Menking et al. 2018). This drying is coincident with Eolian Sand Unit 2 of the Strauss Sand Sheet (Hall and Goble 2015), the aggradation of eolian material as playa filling mud in SHP playas (Holliday et al. 2008), and sand sheet deposits overlying the BWD (Holliday et al. 2001). Though lake level was in decline, there were several modest highstands in the latest Pleistocene, the latest between 11.4 and 9.2 ka., Lake level fall continued post ca.9.0 ka and through the Holocene (Anderson et al. 2002, Menking et al. 2018). This study analyzes the sedimentary architecture, and chronology of deposition in the Monahans eolian system. New investigation has been facilitated by the collection and analysis of eighty deep boreholes (>40 m long), 16 direct-push Geoprobe cores (5-15 m long), and geophysical data including passive seismic and gravity surveys. These data, modeled in three dimensions, provide context and antecedent conditions for this Pleistocene and Holocene sedimentary basin that floors the active Monahans dune field. Direct push Geoprobe core samples yield >95% recovery and preserve intact pedo-sedimentary structure and viable material for optically stimulated luminescence (OSL) dating. Absolute chronology of the stratigraphy has been derived from Single

Aliquot Regeneration OSL (SAR-OSL) protocols on quartz grains extracted from these cores. The results of these analyses provide new insight into sedimentology, sedimentary architecture, pedogenesis and the timing of eolian depositional events for the past 150 ka, since the last interglacial.

Scientific Objectives and Hypotheses

This study has two primary objectives. First, to model the subsurface geometry of late Quaternary deposition and the antecedent fluvial landscape at the contact between the late Ogallala and BWD formations (Fig. 2). This study will provide insight into landscape dynamics at the transition from Miocene/Pliocene mesic conditions to Pleistocene aridity. Second, to test the hypotheses that the pace of eolian deposition and landscape stability is modulated by the extent of the Laurentide Ice Sheet, with wetter periods during Stadials and Interstadials, characterized by pedogenesis or low eolian depositional rates and drier intervals during long interglacials with pronounced eolian activity.

CHAPTER TWO

Methods

Sedimentology, Pedology, and Stratigraphy

We present stratigraphic, sedimentologic, and pedologic observation produced by the analysis of nineteen sediment cores. These cores were collected using the Macro-Core MC7 and MC5 soil sampling systems on a Geoprobe 6620DT. This system employs PVC liners to preserve intact pedo-sedimentary structures for laboratory analysis. Two Macro-core toolsets were used; the wider MC7 toolset (70 mm) was used by default whenever possible and, and the narrower MC5 (38 mm) was employed when challenges to core recovery were encountered, such as dense carbonates, high clay concentrations, or higher pore water pressure below the water table. These sediment-filled liners were moved to the Soils and Sedimentology, Baylor University, Waco TX where they were split lengthwise via a 5 or 7 mm crown cut using a Rockwell F80 Sonicrafter (MC5, MC7 respectively) to access undisturbed sediment while preserving the greatest viable volume for later sampling. Sediment characteristics were then recorded of Munsell Color, grains size, biogenic structures, bedding and pedogenic features including horizon designation (Munsell Color, 2010, NRCS, 2014). Carbonate content was assessed gasometrically by the difference in mass of samples before and after the application of 11% HCl to complete consumption, with samples oven-dried before all mass measurements. Initial grain size observations were augmented by centimeter-scale sampling and analysis with a Malvern Mastersizer 2000, which measures particle sizes from 0.2 to 2000 μm (Rawle

2003). Granulometry samples were collected iteratively with initial spacing of 5 to 20 cm followed by finer spacing (2 to 5 cm) in areas of high variability and stratigraphic unit or soil horizon boundaries. To better measure depositional particle-size ranges, diagenetic and pedogenic carbonate and organic matter components were removed from samples before grain size analysis by the application of 12% hydrogen peroxide followed by 11% HCl respectively. The resultant granulometry data were then divided into classes according to the Wentworth grade scale (Wentworth, 1922). Resultant logs of pedology, granulometry, and carbonate percentage were then used to define depositional units and pedosedimentary facies observed across cores and plotted versus depth in the sedimentary sections.

Optically Stimulated Luminescence Dating

Chronological control of the Geoprobe cores was obtained by OSL dating of quartz grains under Single-Aliquot Regenerative-dose (SAR) protocols which provides an age since the most recent depositional episode of a sample (Wintle and Murray, 2006). OSL relies on the resetting of luminescence signal to a low definable level when subaerially exposed during transport. For this reason, eolian sediments such as those found in the Monahans are advantageous for OSL dating as they receive prolonged (>1 hr) of light exposure during transport and deposition (Mejdahl 1986). Quartz grains were isolated for dating due to their ability to act as a natural dosimeter, and susceptibility to solar resetting (Aitken, 1998). This susceptibility reduces the residual signal inherited from previous depositional episodes to a low definable level.

Single aliquot regeneration (SAR) protocols were used in this study. Each aliquot contained approximately 50 to 150 quartz grains corresponding to a 1-millimeter or less circular diameter of grains adhered (with silicon) to a 1 cm diameter circular aluminum disc. The quartz fraction for a specific grains-size range (e.g. 150-250 μm) with sieving was isolated by density separations using the heavy liquid Na-polytungstate, and at least one 40-minute immersion in hydrofluoric acid (HF 40%), to etch the outer $\sim 10 \mu\text{m}$ of grains, which is affected by alpha radiation (Mejdahl and Christiansen, 1994). The isolated quartz fraction was rinsed finally in HCl (36%) to remove any insoluble fluorides.

The optical purity of quartz separates was tested by exposing aliquots to infrared excitation (1.08 watts from a laser diode at $845 \pm 4 \text{ nm}$), which often preferentially excites feldspar minerals. If this test indicated feldspar contamination, the HF 40-minute immersion was repeated. Another safeguard of quartz grain purity was examination of a small subsample with a visualized petrographic microscope and by Raman spectroscopy. If a subsample exhibited $> 1\%$ non-quartz minerals, particularly feldspar minerals, the sample was retreated with density separations, HF soaking for an additional 20 or 40 minutes, sieved again and recheck for grain purity. The resultant final, prepared samples have a quartz purity of $> 99\%$ and showed weak emissions (< 400 counts/second) with infrared excitation at or close to background counts.

An Automated Risø TL/OSL-DA-15 system was used for SAR analyses. Blue light excitation ($470 \pm 20 \text{ nm}$) was from an array of 30 light-emitting diodes that deliver $\sim 15 \text{ mW/cm}^2$ to the sample position at 90% power. Optical stimulation for all samples was completed at an elevated temperature (125°C) using a heating rate of 5°C/s . All

SAR emissions were integrated for the first 0.8 s of stimulation out of 40 s of measurement, with background emissions integrated for the last ten seconds of data collection, for the 30 to 40 s interval. The luminescence emission for all quartz fractions showed a dominance of a fast component with > 90% diminution of luminescence after 4 seconds of excitation with blue light. The fast ratio was calculated for natural emission and the equivalent emissions for a regenerative dose for each aliquot (Durcan and Duller 2011). Aliquots with a fast ratio of <15 were removed from the final equivalent dose analysis; also, aliquots with infrared depletion ratio of > 5%.

A series of experiments was performed to evaluate the effect of preheating at 160, 180, 200, 220, and 240 °C on isolating the most robust time-sensitive and thermal transfer emissions of the regenerative signal prior to the application of SAR dating protocols. These experiments entailed giving a known dose (10 Gy) and evaluating which preheat resulted in recovery of this dose. There was concordance with the known dose (10 Gy) for preheat temperatures above 180 °C with an initial preheat temperature used of 200 °C for 10 s in the SAR protocols. A second “cut heat” at 200 °C for 10 s was applied prior to the measurement of the test dose. A final heating at 260 °C for 40 s was applied to minimize carryover of luminescence to the succession of regenerative doses. A test for the reproducibility of the radiation-induced SAR ratio (L_x/T_x) was also performed by giving the same beta ($^{90}\text{Sr}/^{90}\text{Yt}$) source radiation exposure for the initial and the final regenerative dose and evaluating the concordance of the SAR ratios, which should be within 10% (Wintle and Murray, 2006).

The equivalent dose (D_e) distributions were log normal and exhibited overdispersion values between 6 and 68%. An overdispersion percentage of a D_e

distribution is an estimate of the relative standard deviation from a central D_e value in context of a statistical estimate of errors (Galbraith and Roberts, 2012). A zero overdispersion percentage indicates high internal consistency in D_e values with 95% of the D_e values within 2σ errors. Overdispersion values $< 20\%$ are routinely assessed for quartz grains that are well solar reset, like aeolian sands and this value is considered a threshold metric for calculation of a D_e value using the central age model (Galbraith and Roberts, 2012; Peng and Forman, 2019). Overdispersion values $>20\%$ indicate mixing or grains of various ages or partial solar resetting of grains; the minimum age model (MAM; four parameters) may be an appropriate statistical treatment for such data. The MAM can effectively model the D_e components that are time dependent and inherited (Galbraith and Roberts, 2012; Peng and Forman, 2019).

The environmental dose rate (D_r) is critical measurement for calculating a luminescence age. The U, Th, Rb and K concentrations are determined on the bulk sediment by inductively coupled plasma mass spectrometry by ALS Laboratories, Reno, NV. The beta and gamma doses were adjusted according to grain diameter to compensate for mass attenuation for the dose rate (Fain et al., 1999). A cosmic ray component, considering location, elevation and depth of strata sampled was calculated which includes the soft component (Prescott and Hutton, 1994; Liang and Forman, 2019). We estimated moisture content (by weight) from present values, particle size characteristics and in reference to field indicators on the height of the water table. The datum year for all OSL ages is AD 2010.

Three-dimensional (3-D) Stratigraphic Modeling of the Monahans

A combination of three-dimensional (3-D) modeling, sedimentary analysis of core samples, and luminescence geochronology yielded enhance architectural insights on the aeolian depositional processes for the Monahans Dune Field in west Texas. Stratigraphic data was collected from sediment cores, borehole cutting logs, and limited geophysical surveys to produce a 3-D model of the subsurface sedimentary architecture. Sixteen sediment cores 5 to 15 m long were used in modeling. Deeper data (20-30 m) are provided by logs of eighty-eight sonic boreholes collected by Westward Environmental, Boerne, TX. Logs of cuttings include lithologic descriptions and depth to observed unit contacts. Observations were recorded at ~1.50 m intervals and at observed changes in lithology. Finally, geophysical data was collected along eight transects with a total length of 5.8 km. Microgravity observations were collected at 50 m spacing with a Scintrex CG-6 Autograv gravity meter with high-precision position measurements collected using a Leica GS18-T kinematic GPS unit (Saibi, 2017). Horizontal to Vertical Spectral Ratio (HSVR) passive seismic sampling was conducted at 100 m spacing in tandem with microgravity using a Tromino Zero 3G+ Seismograph (Chandler and Lively, 2016).

Each of these data sources provided independent observations of the subsurface in varying formats and resolution. Data from all sources was normalized as depth to contact values at the boundaries of four generalized lithologic units. The units: fluvial silty clay w/gravels, silty carbonate rich biogenic playa lake sediments, carbonate soils (stage 3-4 carbonate morphologies (Gile et al., 1966), and aeolian medium to fine sand were first identified in borehole logs and sediments cores. Higher resolution stratigraphy from

Geoprobe cores was reclassified into these broad units with geophysical data recording the density contrast between overlying sediment and the basal fluvial deposits.

The normalized depth data was input into Geosoft Target software (Version 9.6 available through the publisher at <https://www.seequent.com/products-solutions/geosoft-target/>) which produces isosurfaces and voxel block models from drill hole data. Each sample point is recorded in the software as a georeferenced drill hole with depths to each unit contact encountered. Isosurfaces were produced for each unit boundary using a minimum curvature model to interpolate between boreholes. 3D visualization of the subsurface was then produced by populating the area between isosurfaces with 40 m³ voxels (three dimensional pixels). The dimensions of these voxels determine the resolution of the resulting visualization with smaller voxels yielding finer resolution. However, the use of small voxels (< 30 m³) may exceed the sampling density of the minimum curvature method and yield anomalous stratigraphic associations. Initial modeling employs 40 m³ voxels which are fine enough to capture the complexity of lenticular carbonate soils and lake margin deposits but do not exceed sampling resolution.

CHAPTER THREE

Results

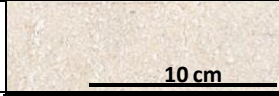
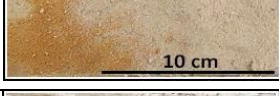
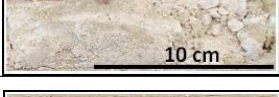
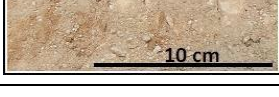
Pedosedimentary Facies for Monahans Eolian Sediments

Five distinct pedosedimentary facies (A, B, C, D, and E) were defined to better characterize the sedimentologic and the pedogenic variability exposed in stratigraphic sections and the Geoprobe cores (Table 1). These facies are the basis for defining depositional sequences and to infer paleoenvironments. Facies are defined by the associated granulometry, bedforms, contact between units, and pedogenic horizons (eg. Bs, Bw, Bt, and Bk). Facies A is an entirely massive, orange to yellowish-brown, well-sorted medium to fine sand (Table 1). This facies is rarely pedogenically modified by weak argillic morphologies. Facies A is associated with eolian reworking of the Blackwater Draw Formation (Holiday 1989, Holiday and Gustavason, 1999, Holiday, 2001). Facies B, another eolian sediment is often coarser than Facies A, composed of yellow to grey very well sorted fine to medium sand with <10% silt. This facies is predominantly massive but unlike A, exhibits millimeter to centimeter bedding in some places. Facies B reflects primary eolian sands, associated with dune movement. Facies C is expressed as a moderately-well to poorly sorted silty sand to sandy silt deposit with 15-55% silt and up to 15% clay (Table 1). Facies C is massive and yellowish-brown in color although secondary rubification associated with groundwater is common. Facies C is a distinct, if rarely observed pedosedimentary facies associated with interdunal environments. Facies D is a poorly sorted light yellow to white silty sand to sandy loam.

This facies (D) (Table 1) is distinctly lighter in color with intercalated moderate to well-developed calcareous soils (Bk) often with well-developed carbonate morphologies (stage 2-4) with common filaments, nodules and induration in some places. This Facies is associated with more surface moisture, reduction in eolian activity and stable and relatively landscape conditions. Facies E is a light brown to yellow moderately well-sorted silty sand to sandy silt. Facies E is notable for the presence of incipient ped soil structure illuviated clays, upward fining sequences, and other pedogenic features associated with Bw, Bs, and Bt soil horizonation. This pedo-sedimentary complex is associated with prolonged landscape stability. The upper contacts of this facies is often rubified with argillic soils and are abruptly truncated indicating sequentially subaerial exposure, landform stabilization, and subsequent erosion.

Examples of this facies in some localities exhibit clay lamellae (Table 1).

Table 1. Pedo-sedimentary facies of Monahans cores

Facies	Core Photo	Texture	Sedimentary Structure	Associated Soil Horizonation	Depositional Environment/Processes
A		Well-sorted orange to yellowish-brown medium sand to silty sand	Massive	C, N/A	Eolian reworking of Blackwater Draw Sediments
B		Very well-sorted light yellow to grey fine to medium sand	Massive to finely bedded	C, N/A	Primary Eolian Sand, associated with dune movement
C		Moderately well to poorly-sorted silty sand to sandy silt	Massive with Fe staining	Bw, Bt	Interdunal deposition
D		Poorly sorted light yellow to white silty sand to sandy loam	Stage 2 to 4 carbonate with common nodules to induration	Bk	Pedo-sedimentary complex associated with wet conditions
E		Moderately well-sorted silty sand to sandy silt	Massive, pedogenic features including clay illuviation, upward fining sequences	Bw, Bs, Bt	Pedo-sedimentary complex associated with prolonged stability

Logs of Sonic Borings

The exploratory sampling for this study involved the collection of eighty-four sonic borings (Fig. 3). which were logged at ~1.5 m intervals and at observed changes in lithology (Fig. 4). The boring data is propriety information from Atlas Sand Inc. (Austin, TX)

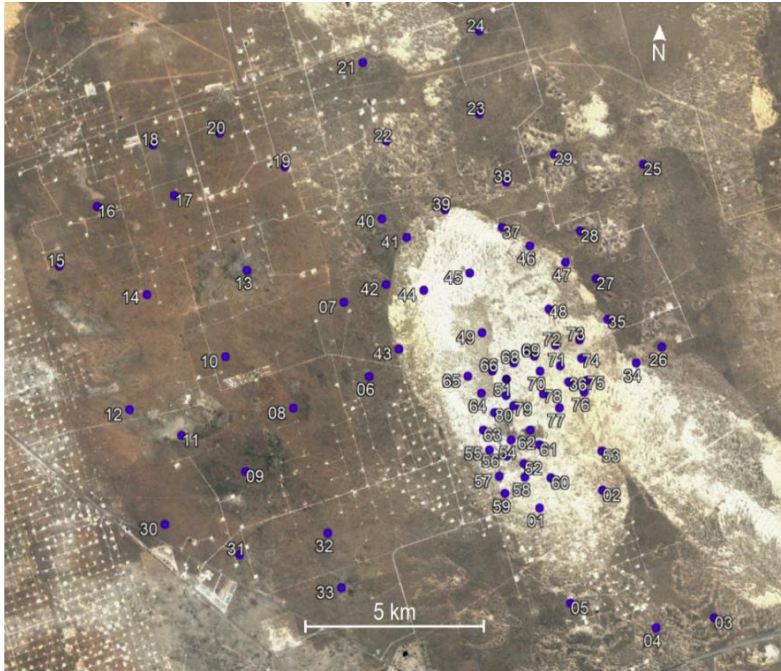


Figure 3. Locations of Sonic Boreholes collected in the Monahans dune field. Borehole locations marked in blue.

provided gratis for this research as part as cooperative research agreement. These borings were most concentrated in the topographically high region in the center of the study area, with active barchanoid dunes. Several borings were also taken from the peripheral sand sheet to the west and east but more widely spaced than borings from the active dune system (Fig. 3). Those borings which extend $> \sim 35$ m depth often retrieve a basal deposit of a clay-rich red alluvial deposit with pedogenic carbonate and clastic material. The upper surface of this unit is shallower in the northeast with an apparent dip to the southwest. Above this contact, the borings reveal the Blackwater Formation (BDF) of eolian sediment with variations in color and texture associated with pedogenesis (Gustavson et al., 1991., Gustavson and Holliday, 1999). The borings west of the active dune field encounter two forms of carbonate: moderate to well-developed carbonate

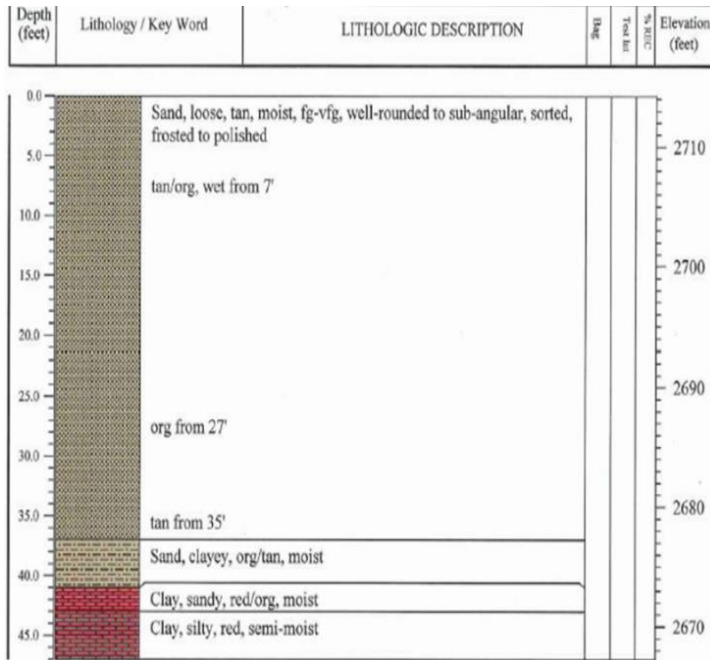


Figure 4. Log of cuttings collected from Sonic Borehole AT2-17-1. The log describes color, texture, and moisture of sediments with recorded depths of diagnostic changes.

paleosols (Stage II-IV) which is observed elsewhere in the study area, and an indurated cohesive deposit which in part correlates with palustrine beds exposed in a nearby quarry (Wiest et al., 2020). There appears to be a topographic inversion in which the BDF infills into an elongate northwest to southeast trending slope and depression, resulting in the highest dunes on the surface.

However, this and other spatial interpolations are better defined through 3D modeling of borehole data.

Geoprobe Sediment Cores

Using the preliminary trends observed in sonic boring logs along with near-surface geological features, Geoprobe cores collected were organized into three broad field context. The first field area (A) is a pronounced topographic high associated with currently active dunes, interdunal depressions, and poorly vegetated barchanoid ridge dune forms (Fig. 5). Field area B to the northeast is currently topographically lower than A, however the basal alluvium is at its shallowest depth potentially indicating a paleo high. This area closest to the High Plains Escarpment with a moderately vegetated sand

sheet and parabolic dune forms. The final field area (C) is composed of sand sheets and parabolic dunes to the west of the dune mass and was distinguished by near-surface meters-thick carbonate lithologies observable in bore logs, Geoprobe cores, and exposed by gravel mining. Ages constraining depositional units were collected by OSL and TT-OSL under SAR protocols (Table 2.)

Table 2: Optically stimulated luminescence (OSL) ages on quartz grains from geoprobe cores and outcrop in the Monahans dune field

Core/drive/ depth (cm)	Lab number	Aliquots ^a	Grain Size (μm)	Equivalent dose (Gray) ^b	Over- dispersion (%) ^c	U (ppm) ^d	Th (ppm) ^d	K (%) ^d	H ₂ O	Cosmic Dose rate (mGray/yr)	Dose rate (mGray/yr)	OSL age (yr) ^e
MON17-1B 68	BG4591	41/42	250-150	1.00 ± 0.09	35 ± 4	0.34 ± 0.01	0.94 ± 0.01	0.18 ± 0.01	5 ± 2	0.191 ± 0.019	0.50 ± 0.02	2010 ± 210
MON17-1C 20	BG4592	32/34	250-150	0.98 ± 0.05	20 ± 3	0.48 ± 0.01	1.54 ± 0.01	0.30 ± 0.01	5 ± 2	0.176 ± 0.018	0.66 ± 0.03	3535 ± 175
MON17-1D 10	BG4593	33/35	250-150	7.00 ± 0.30	21 ± 3	0.47 ± 0.01	1.33 ± 0.01	0.23 ± 0.01	10 ± 2	0.149 ± 0.015	0.55 ± 0.03	12,765 ± 870
MON17-1D 72	BG4769	33/35	355-250	9.37 ± 0.36	24 ± 2	0.38 ± 0.01	1.08 ± 0.01	0.31 ± 0.01	10 ± 2	0.147 ± 0.015	0.51 ± 0.03	18,300 ± 930
MON17-1F 15	BG4594	35/35	250-150	21.08 ± 1.04	20 ± 2	0.40 ± 0.01	1.09 ± 0.01	0.21 ± 0.01	10 ± 2	0.115 ± 0.011	0.46 ± 0.03	45,365 ± 3320
MON17-1F 96	BG4595	27/30	250-150	58.47 ± 2.70	21 ± 3	0.49 ± 0.01	1.17 ± 0.01	0.34 ± 0.01	15 ± 5	0.112 ± 0.011	0.56 ± 0.02	103,960 ± 6240
MON17-1F 96	BG4595T T	32/35	250-150	54.25 ± 2.71	17 ± 3	0.49 ± 0.01	1.17 ± 0.01	0.34 ± 0.01	15 ± 5	0.112 ± 0.011	0.56 ± 0.02	96,450 ± 6080
MON17-1G 56	BG4596	30/35	250-150	106.32 ± 4.12	18 ± 3	0.38 ± 0.01	1.08 ± 0.01	0.21 ± 0.01	15 ± 5	0.103 ± 0.010	0.43 ± 0.02	245,610 ± 13,510
MON17-1G 56	BG4596T T	15/17	250-150	00.87 ± 18.0	24 ± 5	0.38 ± 0.01	1.08 ± 0.01	0.21 ± 0.01	15 ± 5	0.103 ± 0.010	0.43 ± 0.02	241,820 ± 18,970
MON17-2A 40	BG4671	27/30	250-150	0.060 ± 0.010	58 ± 11	0.32 ± 0.01	0.81 ± 0.01	0.62 ± 0.01	3 ± 1	0.244 ± 0.024	0.97 ± 0.03	60 ± 10
MON17-2E 30	BG4714	37/45	250-150	0.36 ± 0.02	23 ± 3	0.44 ± 0.01	0.92 ± 0.01	0.22 ± 0.01	7 ± 2	0.207 ± 0.021	0.56 ± 0.03	640 ± 35
MON17-2D 15	BG4696	38/40	250-150	2.59 ± 0.12	17 ± 2	0.42 ± 0.01	1.20 ± 0.01	0.28 ± 0.01	10 ± 3	0.158 ± 0.016	0.53 ± 0.03	4925 ± 275
MON17-2E 30	BG4672	38/40	250-150	5.93 ± 0.010	13 ± 2	0.49 ± 0.01	1.43 ± 0.01	0.26 ± 0.01	10 ± 3	0.136 ± 0.014	0.53 ± 0.03	11,080 ± 785
MON17-2F 10	BG4673	35/39	250-150	32.96 ± 1.61	19 ± 2	0.54 ± 0.01	2.76 ± 0.01	0.25 ± 0.01	10 ± 3	0.1222 ± 0.012 0.03	0.62 ±	52,875 ± 3690
MON17-2F 78	BG4715	40/45	250-150	23.26 ± 1.09	19 ± 2	0.35 ± 0.01	0.97 ± 0.01	0.14 ± 0.01	10 ± 3	0.113 ± 0.011	0.37 ± 0.02	62,760 ± 3870
MON17-2H 68	BG4674	39/40	250-150	36.44 ± 1.27	17 ± 2	0.56 ± 0.01	1.58 ± 0.01	0.28 ± 0.01	10 ± 3	0.091 ± 0.009	0.55 ± 0.03	66,865 ± 4475
MON17-3B 70	BG4559	32/34	250-150	13.92 ± 0.58	12 ± 3	0.51 ± 0.01	1.35 ± 0.01	0.26 ± 0.01	5 ± 2	0.183 ± 0.018	0.59 ± 0.03	23,365 ± 1570
MON17-3D 60	BG4561	29/35	250-150	25.76 ± 1.17	22 ± 3	0.32 ± 0.01	0.92 ± 0.01	0.17 ± 0.01	10 ± 2	0.138 ± 0.014	0.42 ± 0.03	61,260 ± 4020
MON17-3E 70	BG4679	39/40	250-150	33.76 ± 1.43	24 ± 3	0.51 ± 0.01	1.17 ± 0.01	0.30 ± 0.01	15 ± 5	0.130 ± 0.013	0.55 ± 0.03	61,200 ± 3840
MON17-3F 93	BG4563T T	19/20	250-150	15.68 ± 17.0	15 ± 3	0.58 ± 0.01	4.45 ± 0.01	0.58 ± 0.01	15 ± 5	0.113 ± 0.011	0.89 ± 0.04	464,530 ± 29,810
MON17-4C 82	BG4688	36/40	355-250	0.26 ± 0.04	55 ± 7	0.26 ± 0.01	0.72 ± 0.01	0.11 ± 0.01	10 ± 3	0.166 ± 0.016	0.35 ± 0.03	720 ± 110
MON17-5A 35	BG4685	31/39	250-150	1.44 ± 0.08	24 ± 3	0.70 ± 0.01	0.72 ± 0.01	0.20 ± 0.01	5 ± 2	0.254 ± 0.025	0.61 ± 0.03	2350 ± 140
MON17-5B-70	BG4686	34/40	250-150	8.17 ± 0.46	25 ± 3	0.59 ± 0.01	1.27 ± 0.01	0.32 ± 0.01	10 ± 3	0.19 ± 0.02 0.03	0.61 ±	13,025 ± 855

Table 2: Optically stimulated luminescence (OSL) ages on quartz grains from geoprobe cores and outcrop in the Monahans dune field “continued”

Core/drive/ depth (cm)	Lab number	Aliquots ^a	Grain Size (μm)	Equivalent dose (Gray) ^b	Over- dispersion (%) ^c	U (ppm) ^d	Th (ppm) ^d	K (%) ^d	H ₂ O	Cosmic Dose rate (mGray/yr)	Dose rate (mGray/yr)	OSL age (yr) ^e
MON17-5H 60	BG4684	27/30	250-150	>200	NA	0.81 \pm 0.01	1.88 \pm 0.01	0.32 \pm 0.01	10 \pm 3	0.089 \pm 0.009	0.65 \pm 0.03	307,430 \pm 23,320
MON17-6E 90	BG4626	32/35	250-150	0.19 \pm 0.01	50 \pm 7	0.21 \pm 0.01	0.63 \pm 0.01	0.22 \pm 0.01	5 \pm 2	0.126 \pm 0.13	0.39 \pm 0.03	470 \pm 20
MON17-7A 100	BG4508	72/73	250-150	4.93 \pm 0.66	37 \pm 3	0.81 \pm 0.01	2.47 \pm 0.01	0.77 \pm 0.01	5 \pm 2	0.214 \pm 0.021	1.15 \pm 0.03	4280 \pm 480
MON17-7F 75	BG4510	44321	250-150	>210	NA	0.56 \pm 0.01	1.98 \pm 0.01	0.39 \pm 0.01	10 \pm 2	0.079 \pm 0.008	0.65 \pm 0.04	>320,000
MON17-7F 75	BG4510T T	19/20	250-150	00.52 \pm 19.8	18 \pm 4	0.53 \pm 0.01	1.98 \pm 0.01	0.39 \pm 0.01	15 \pm 5	0.102 \pm 0.010	0.65 \pm 0.02	616,950 \pm 43,380
MON17-7G 70	BG4517	35/35	250-150	>210	NA	0.56 \pm 0.01	1.99 \pm 0.01	0.27 \pm 0.01	15 \pm 5	0.075 \pm 0.007	0.59 \pm 0.03	>300,000
MON17-7H 57	BG4500	26/35	250-150	>161	NA	0.53 \pm 0.01	2.01 \pm 0.01	0.51 \pm 0.01	15 \pm 5	0.090 \pm 0.009	0.67 \pm 0.03	>240,000
MON17-8A 65	BG4491	34/35	250-150	11.97 \pm 0.50	21 \pm 3	0.52 \pm 0.01	1.49 \pm 0.01	0.27 \pm 0.01	7 \pm 2	0.208 \pm 0.021	0.63 \pm 0.02	19,280 \pm 935
MON17-8B 50	BG4490	33/35	250-150	14.42 \pm 0.48	15 \pm 2	0.52 \pm 0.01	1.49 \pm 0.01	0.27 \pm 0.01	10 \pm 2	0.175 \pm 0.016	0.60 \pm 0.02	24,110 \pm 995
MON17-8C 70	BG4492	33/35	250-150	12.86 \pm 0.64	20 \pm 3	0.39 \pm 0.01	1.29 \pm 0.01	0.19 \pm 0.01	10 \pm 2	0.166 \pm 0.015	0.49 \pm 0.01	26,010 \pm 1450
MON17-8E 70	BG4501	33/35	250-150	15.93 \pm 0.81	22 \pm 3	0.35 \pm 0.01	0.90 \pm 0.01	0.17 \pm 0.01	10 \pm 2	0.123 \pm 0.012	0.42 \pm 0.01	45,525 \pm 2440
MON17-8F 70	BG4502	33/35	250-150	22.61 \pm 0.90	19 \pm 2	0.36 \pm 0.01	0.98 \pm 0.01	0.24 \pm 0.01	10 \pm 2	0.115 \pm 0.011	0.42 \pm 0.01	53,280 \pm 2520
MON17-8G 70	BG4515	33/35	250-150	38.46 \pm 1.39	17 \pm 2	0.54 \pm 0.01	1.46 \pm 0.01	0.46 \pm 0.01	15 \pm 5	0.104 \pm 0.010	0.68 \pm 0.01	56,560 \pm 3390
MON17-8G 70	BG4515T T	37/50	250-150	41.04 \pm 2.01	25 \pm 4	0.54 \pm 0.01	1.46 \pm 0.01	0.46 \pm 0.01	15 \pm 5	0.104 \pm 0.010	0.68 \pm 0.01	60,350 \pm 4220
MON17-8H 40	BG4503	30/35	250-150	>162	NA	0.61 \pm 0.01	2.20 \pm 0.01	0.40 \pm 0.01	10 \pm 2	0.094 \pm 0.009	0.67 \pm 0.01	>235,000
MON17-8I 6	BG4571	21/23	250-150	>230	NA	0.65 \pm 0.01	3.75 \pm 0.01	0.63 \pm 0.01	15 \pm 5	0.091 \pm 0.009	0.88 \pm 0.04	>260,000
MON17-8I 6	BG4571T T	27/31	250-150	39.22 \pm 16.6	24 \pm 3	0.65 \pm 0.01	3.75 \pm 0.01	0.63 \pm 0.01	15 \pm 5	0.091 \pm 0.009	0.88 \pm 0.04	379,600 \pm 26,780
MON18-12A 25	BG4707	20/45	250-150	<0.02	NA	0.24 \pm 0.01	0.61 \pm 0.01	0.14 \pm 0.01	5 \pm 2	0.258 \pm 0.026	0.46 \pm 0.03	<40
MON18-12B 20	BG4708	40/45	250-150	0.29 \pm 0.02	36 \pm 5	0.26 \pm 0.01	0.75 \pm 0.01	0.15 \pm 0.01	7 \pm 2	0.206 \pm 0.021	0.42 \pm 0.02	675 \pm 55
MON18-12C 55	BG4709	35/40	250-150	0.29 \pm 0.03	35 \pm 5	0.28 \pm 0.01	0.72 \pm 0.01	0.18 \pm 0.01	10 \pm 2	0.177 \pm 0.018	0.44 \pm 0.02	660 \pm 65
MON18-12C 55	BG4710	45/59	250-150	19.72 \pm 0.93	22 \pm 2	0.28 \pm 0.01	0.71 \pm 0.01	0.35 \pm 0.01	10 \pm 2	0.163 \pm 0.016	0.57 \pm 0.02	34,470 \pm 1695

Table 2: Optically stimulated luminescence (OSL) ages on quartz grains from geoprobe cores and outcrop in the Monahans dune field “continued”

Core/drive/ depth (cm)	Lab number	Aliquots ^a	Grain Size (μm)	Equivalent dose (Gray) ^b	Over- dispersion (%) ^c	U (ppm) ^d	Th (ppm) ^d	K (%) ^d	H ₂ O	Cosmic Dose rate (mGray/yr)	Dose rate (mGray/yr)	OSL age (yr) ^e
MON18-13A 22	BG4703	24/36	250-150	0.03 ± 0.01	131 ± 43	0.25 ± 0.01	0.91 ± 0.01	0.17 ± 0.01	5 ± 2	0.256 ± 0.026	0.50 ± 0.02	55 ± 15
MON18-13A 50	BG4720	31/47	250-150	0.30 ± 0.01	22 ± 4	0.25 ± 0.01	0.63 ± 0.01	0.08 ± 0.01	5 ± 2	0.217 ± 0.022	0.39 ± 0.02	770 ± 60
MON18-13E 45	BG4704	51/55	250-150	0.44 ± 0.04	75 ± 8	0.34 ± 0.01	1.01 ± 0.01	0.24 ± 0.01	10 ± 2	0.133 ± 0.013	0.49 ± 0.02	895 ± 85
MON18-13F 70	BG4705	33/39	250-150	69.48 ± 6.46	18 ± 3	0.53 ± 0.01	1.86 ± 0.01	0.34 ± 0.01	15 ± 5	0.114 ± 0.011	0.59 ± 0.02	287,060 ± 14,580
MON18-14B 25	BG4744	35/51	355-250	<0.01	NA	0.46 ± 0.01	0.59 ± 0.01	0.06 ± 0.01	5 ± 2	0.205 ± 0.021	0.38 ± 0.01	<20
MON18-14C 15	BG4751	32/40	355-250	20.46 ± 0.82	19 ± 3	1.01 ± 0.01	1.31 ± 0.01	0.24 ± 0.01	10 ± 2	0.179 ± 0.018	0.67 ± 0.02	30,560 ± 1440
MON18-14D 75	BG4743	37/39	355-250	34.16 ± 1.60	18 ± 2	0.65 ± 0.01	1.09 ± 0.01	0.19 ± 0.01	10 ± 2	0.146 ± 0.015	0.51 ± 0.02	67,300 ± 3850
MON18-17A 60	BG4697	39/40	250-150	3.90 ± 0.01	19 ± 2	0.51 ± 0.01	1.41 ± 0.01	0.39 ± 0.01	7 ± 2	0.215 ± 0.022	0.71 ± 0.02	5480 ± 290
MON18-17B 55	BG4653	39/40	250-150	9.65 ± 0.01	23 ± 3	0.80 ± 0.01	2.02 ± 0.01	0.56 ± 0.01	10 ± 2	0.196 ± 0.020	0.98 ± 0.02	9840 ± 480
MON18-17D 07	BG4654	39/40	250-150	45.68 ± 2.00	24 ± 3	0.48 ± 0.01	1.16 ± 0.01	0.52 ± 0.01	15 ± 5	0.158 ± 0.016	0.68 ± 0.03	66,800 ± 4110
MON18-17E 05	BG4648	35/40	250-150	14.17 ± 4.57	20 ± 3	0.42 ± 0.01	1.17 ± 0.01	0.34 ± 0.01	15 ± 5	0.137 ± 0.014	0.57 ± 0.02	192,390 ± 11,790
MON18-17E 05	BG4648T T	22/23	250-150	07.72 ± 5.79	20 ± 3	0.42 ± 0.01	1.17 ± 0.01	0.34 ± 0.01	15 ± 5	0.137 ± 0.014	0.57 ± 0.02	187,400 ± 12,500
MON18-17F 07	BG4647	37/40	250-150	>160	NA	1.01 ± 0.01	1.31 ± 0.01	2.06 ± 0.01	15 ± 5	0.124 ± 0.012	0.71 ± 0.02	>220,000
MON18-17F 85	BG4646	20/44	250-150	>150	NA	0.98 ± 0.01	3.69 ± 0.01	0.75 ± 0.01	15 ± 5	0.112 ± 0.011	1.05 ± 0.03	>150,000
MON18-17F 85	BG4646T T	22/23	250-150	66.63 ± 17.2	20 ± 5	0.98 ± 0.01	3.69 ± 0.01	0.75 ± 0.01	15 ± 5	0.112 ± 0.011	1.05 ± 0.03	254,750 ± 21,170
MON19-30-B7	BG4994	36/38	250-150	9 ± 0.86	33 ± 4	0.38 ± 0.01	1.11 ± 0.01	0.27 ± 0.01	5 ± 3	0.13 ± 0.01	0.5 ± 0.02	18,125 ± 1,815
MON19-30- D40	BG4993	37/50	250-150	100 ± 4.99	19 ± 3	0.59 ± 0.01	1.71 ± 0.01	0.54 ± 0.01	15 ± 5	0.16 ± 0.02	0.76 ± 0.03	132,430 ± 8,860
MON19-30- F75	BG4995T T	15/16	250-150	84.46 ± 7.93	45 ± 9	0.49 ± 0.01	1.49 ± 0.01	0.31 ± 0.01	30 ± 5	0.20 ± 0.02	0.44 ± 0.02	273,960 ± 19,760
MON19-30- L120	BG4998T T	5/19	250-150	30.19 ± 10.6	6 ± 5	0.78 ± 0.01	2.37 ± 0.01	0.62 ± 0.01	10 ± 5	0.05 ± 0.02	0.81 ± 0.03	525,590 ± 37,970

Table 2: Optically stimulated luminescence (OSL) ages on quartz grains from geoprobe cores and outcrop in the Monahans dune field “continued”

Core/drive/ depth (cm)	Lab number	Aliquots ^a	Grain Size (µm)	Equivalent dose (Gray) ^b	Over-dispersion (%) ^c	U (ppm) ^d	Th (ppm) ^d	K (%) ^d	H ₂ O	Cosmic Dose rate (mGray/yr)	Dose rate (mGray/yr)	OSL age (yr) ^e
MON19-31A-75	BG5001	38/40	250-150	11.67 ± 1.1	24 ± 3	0.67 ± 0.01	1.8 ± 0.01	0.57 ± 0.01	10 ± 5	0.13 ± 0.013	0.88 ± 0.04	13,300 ± 1,390
MON19-31B-40	BG5002	39/40	250-150	37.33 ± 1.8	19 ± 2	1.07 ± 0.01	1.82 ± 0.01	0.61 ± 0.01	10 ± 3	0.16 ± 0.02	0.98 ± 0.03	38,050 ± 2,195
MON19-31D-81	BG5003	38/40	355 - 250	62.25 ± 5.97	47 ± 6	0.53 ± 0.01	1.86 ± 0.01	0.37 ± 0.01	5 ± 3	0.14 ± 0.01	0.65 ± 0.02	96,050 ± 10,120
MON19-31D-128	BG5021	18/20	250-150	59.23 ± 11.7	29 ± 5	0.89 ± 0.01	2.8 ± 0.01	0.93 ± 0.01	15 ± 5	0.13 ± 0.01	1.12 ± 0.05	357,300 ± 26,400
MON19-MINE1-D	BG4761TT	21/23	250-150	188.81 ± 9.8	21 ± 4	2.2 ± 0.01	0.97 ± 0.01	0.27 ± 0.1	10 ± 3	0.23 ± 0.02	0.95 ± 0.03	198,660 ± 12,140
MON-MINE1-E	BG4765TT	25/25	250-150	46.93 ± 15.7	21 ± 3	1.52 ± 0.01	2.32 ± 0.01	0.62 ± 0.01	15 ± 5	0.14 ± 0.01	1.03 ± 0.05	237,520 ± 15,360
MON-MINE1-B	BG4760TT	29/33	250-150	10.04 ± 18.0	29 ± 4	5.1 ± 0.01	0.71 ± 0.01	0.23 ± 0.01	10 ± 3	0.16 ± 0.02	1.45 ± 0.05	334,610 ± 22,240

^aAliquots used in equivalent dose calculations versus original aliquots measured.

^bEquivalent dose calculated on a pure quartz fraction with about 40-100 grains/aliquot and analyzed under blue-light excitation (470 ± 20 nm) by single aliquot regeneration protocols (Murray and Wintle, 2003). The central age model of Galbraith et al. (1999) was used to calculate equivalent dose when overdispersion

values are <25% (at one sigma errors; a finite mixture model was used with overdispersion values >25% to determine the youngest equivalent dose population. ^cValues reflect precision beyond instrumental errors; values of ≤ 25% (at 1 sigma limit) indicate low dispersion in equivalent dose values and an unimodal distribution.

^dU, Th and K content analyzed by inductively-coupled plasma-mass spectrometry analyzed by ALS Laboratories, Reno, NV; U content includes Rb equivalent. includes also a cosmic dose rate calculated from parameters in Prescott and Hutton (1994).

^eSystematic and random errors calculated in a quadrature with 1000 Monte Carlo simulations and at one standard deviation. Datum year is AD 2010. After Tew-Todd et al., 2020

Field Area A

Field Area A is defined by its elevation which is up to 25 m above the neighboring sand sheet. This area constitutes the active dune field in the Monahans eolian system, and is characterized by little vegetation cover, often < 10%. The eolian surface is composed of predominantly barchanoid, and transverse dune forms oriented perpendicular to the southeast wind which predominates in the summer months (Machenberg, 1984). Interdunal depressions, topographically lower by 5 to 20 m than dune crests, appear to be areas of deflation and net erosion, often with a coarser sand lag. Interdune deflation areas often exposed more cohesive sediments of reddish Facies A type, or wet areas, often with vegetation, indicating a near surface water table. Field region A contains the thickest deposits of active to most recent (< 2 ka old) eolian deposition. Geoprobe cores across all three regions were collected to the maximum depth achieved often limited by the hardness and cohesion of sediments at depths > 10 m. However, in region A coring depth was limited by a high-water table, artesian pressure which often resulted in liquefaction of sands with coring and poor recovery.

Cores in area A reveal the youngest evidence (< 1 ka) for eolian deposition with surprisingly considerably older sediments ca. 30 to 300 ka old beneath (Fig 5). The deepest and oldest aeolian sediment retrieved in core MON18-13 (unit 1) was a fine and well sorted Facies B type-sediment that yielded an OSL age of $287,060 \pm 14,580$ (BG4705). The uppermost 0.80 m of this unit (1) has been extensively pedogenically modified with significant rubification and common lamellae that were truncated subsequently (Figure 5). Overlying this oldest sediment is coarser-grain facies B type-sediment (unit 2) with millimeter-scale bedding at the base. This upper unit 2 exceeds 5

m thickness and yielded OSL ages near the bottom and top of 895 ± 85 (BG4704) and 920 ± 55 yr (BG4704), respectively, with the most recent sand (unit 3) 30 cm from the

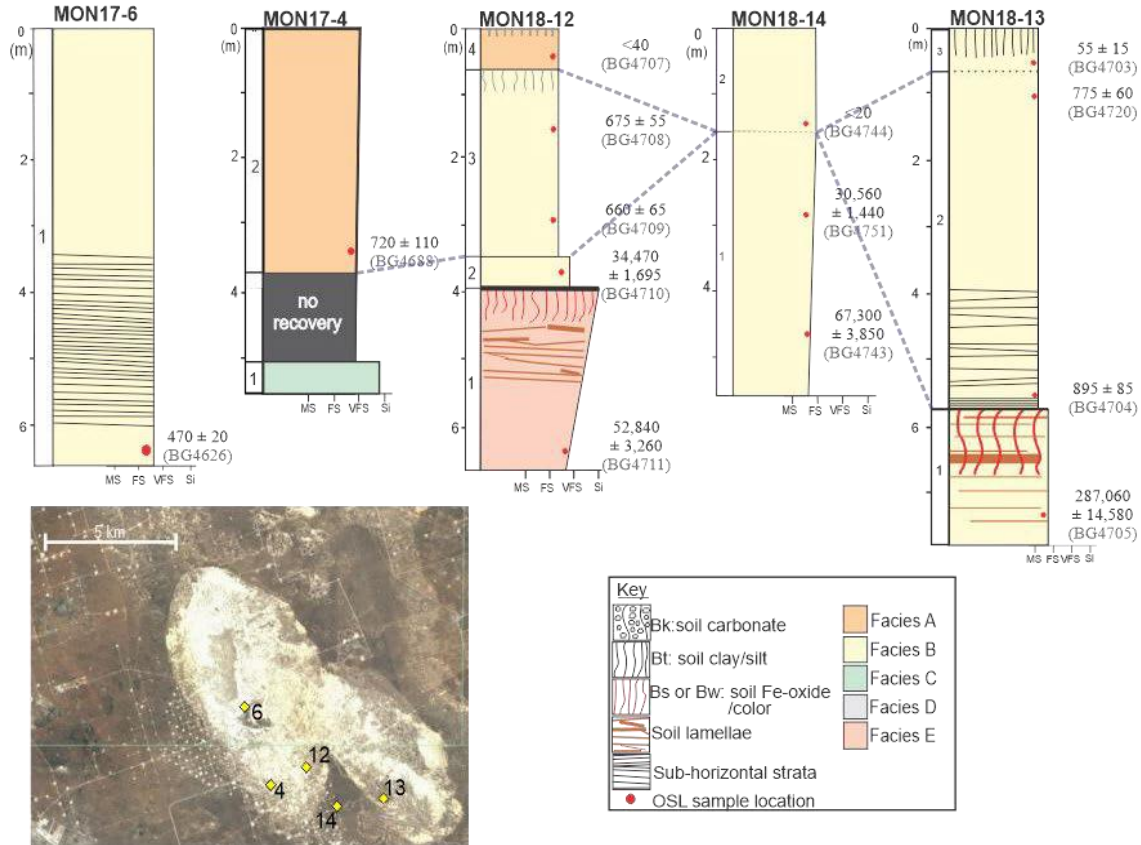


Figure 5. Stratigraphy of geoprobe cores collected from field area A with core locations inset.

surface returning an OSL age of 55 ± 15 yr (BG4703). In Area A eolian sand that spans the past 1 ka are found in all cores, though in cores MON18-12 and MON18-14 have sediment that is < 40 yr old, indicating contemporary eolian activity.

The number of facies in Core MON18-12 is a notable exception for cores in area A. This core at depth (unit 1) exhibits a fine-grained variant of Facies E with considerable translocation of silt and clay in the upper 1 m, distinct rubification, and truncation at unit upper boundary. OSL ages on quartz grains from eolian sediment below pedogenic

modification of $52,840 \pm 3260$ (BG4711) and from the overlying unit 2 of $34,470 \pm 1695$ (BG4710) indicates a maximum period of pedogenesis of ca. 19 ka. A unique discovery is the occurrence of Facies C, possibly a clay rich interdunal pond deposit in the base of MON17-4, which is > 720 yr old.

Field Area B

Field Area B is located to the northwest of A and is dominated at the surface by a moderately vegetated sand sheets (Fig. 6). Initial exploration via sonic borings reveal complex series of carbonate paleosols, and a shallower depth to the alluvial basement than in area A. Five Geoprobe cores were recovered from this region between 9 and 19 m long.

Cores in Area B include well-developed carbonate paleosols indicative of prolonged periods of stability buried by 5 to 10 m of eolian sands. The only core in this region to penetrate deeper than 9 m was MON19-30 with nearly full recover to nearly 19 m. The deepest units of this core are composed of a Facies E silty sand overlain by massive facies B material which yielded a TT-OSL age of $554,420 \pm 40,340$ yr (BG4997TT). Most cores show >1 m thick carbonate-rich Facies D of pedogenic origin (Fig. 6). Luminescence ages on eolian sediment beneath these soils and above indicate varying periods of landscape stability. This complex series of Facies D units are overlain by 6 to 10 m of eolian sand. The oldest of these units is found in core MON17-8 where a fine-grained Facies E sandy silt yielded a TT-OSL age of $379,600 \pm 26,780$ (BG4571TT), which exhibits >1 m thick cambic horizon of and a distinct erosional upper contact. Above this contact is a 6 m unit of primary eolian sand with a basal age of $64,270 \pm 4,050$ (BG4515TT). Corollary units are found in neighboring cores MON17-3 and

MON17-2 both of which have Facies B massive eolian units with basal ages of $61,200 \pm 3,840$ (BG4679) and $66,870 \pm 4,475$ (BG4674) respectively. Rubified facies A sediment is abundant at the surface across region B in all cores except for core MON19-30 which has massive medium sands at the surface. All cores from area B are capped by a series of eolian units deposited in the past 70 ka; with OSL ages <1 ka for the upper 2 m of cores MON17-1 and MON17-2.

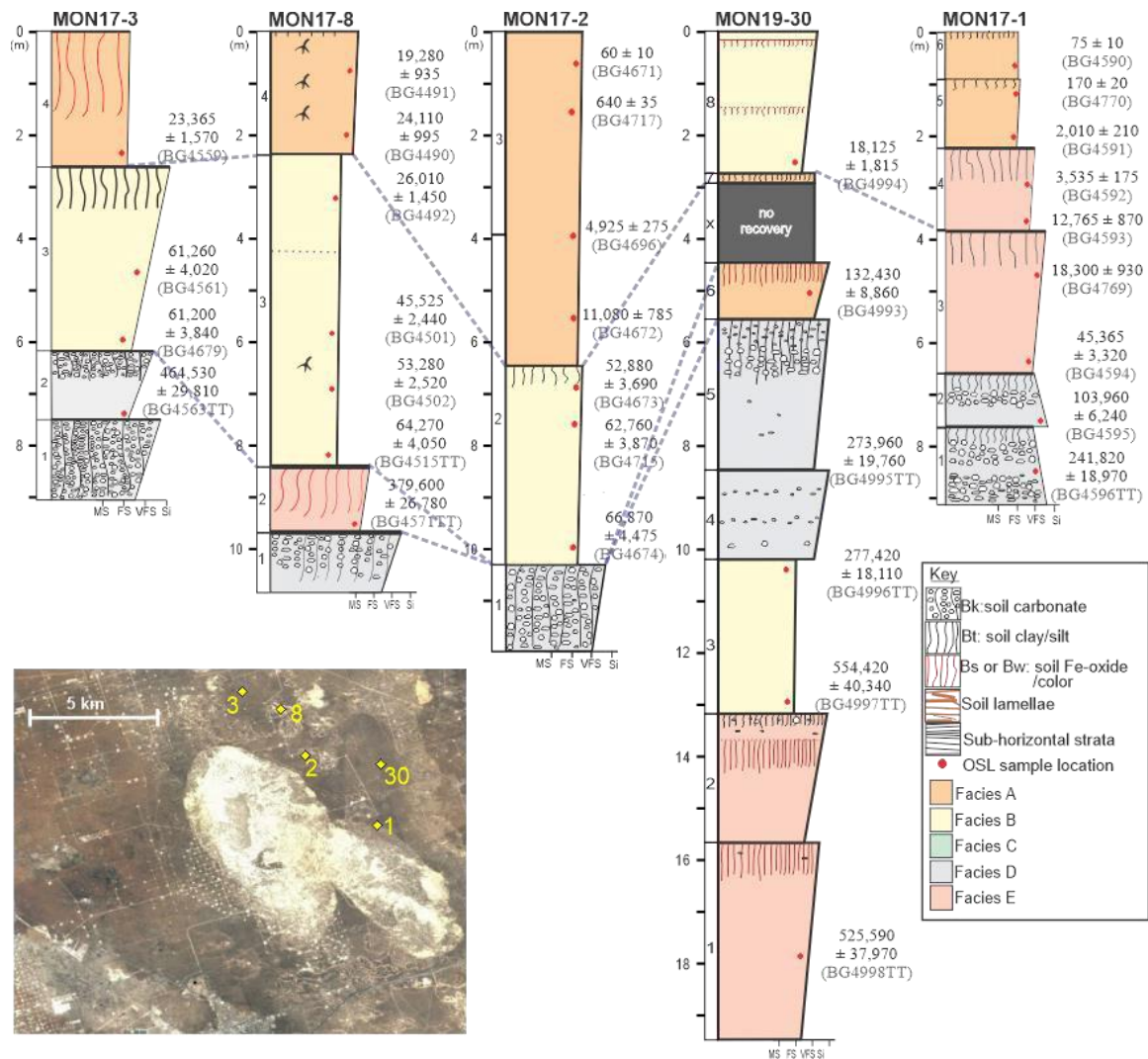


Figure 6. Stratigraphy of geoprobe cores collected from field area B with core locations inset.

Field Area C

Field Area C is distinguished by the transition from eolian depositional environments to near-surface palustrine deposits and compound carbonate paleosols. Core MON17-7 and MON19-31 both penetrate complex series of indurated facies D sediment into massive eolian sand dated in core MON17-7 to $515,740 \pm 33,240$ (BG4524TT). Three cores include multiple carbonate-rich depositional units. OSL ages from these units span from $254,760 \pm 21,170$ (BG4646TT) to $22,750 \pm 1,575$ (BG4518). Core MON17-5 is the easternmost core in this field area which includes silty medium-sand facies A with two OSL ages of $307,430 \pm 23,320$ (BG4684) and $309,420 \pm 22,100$ (BG4683).

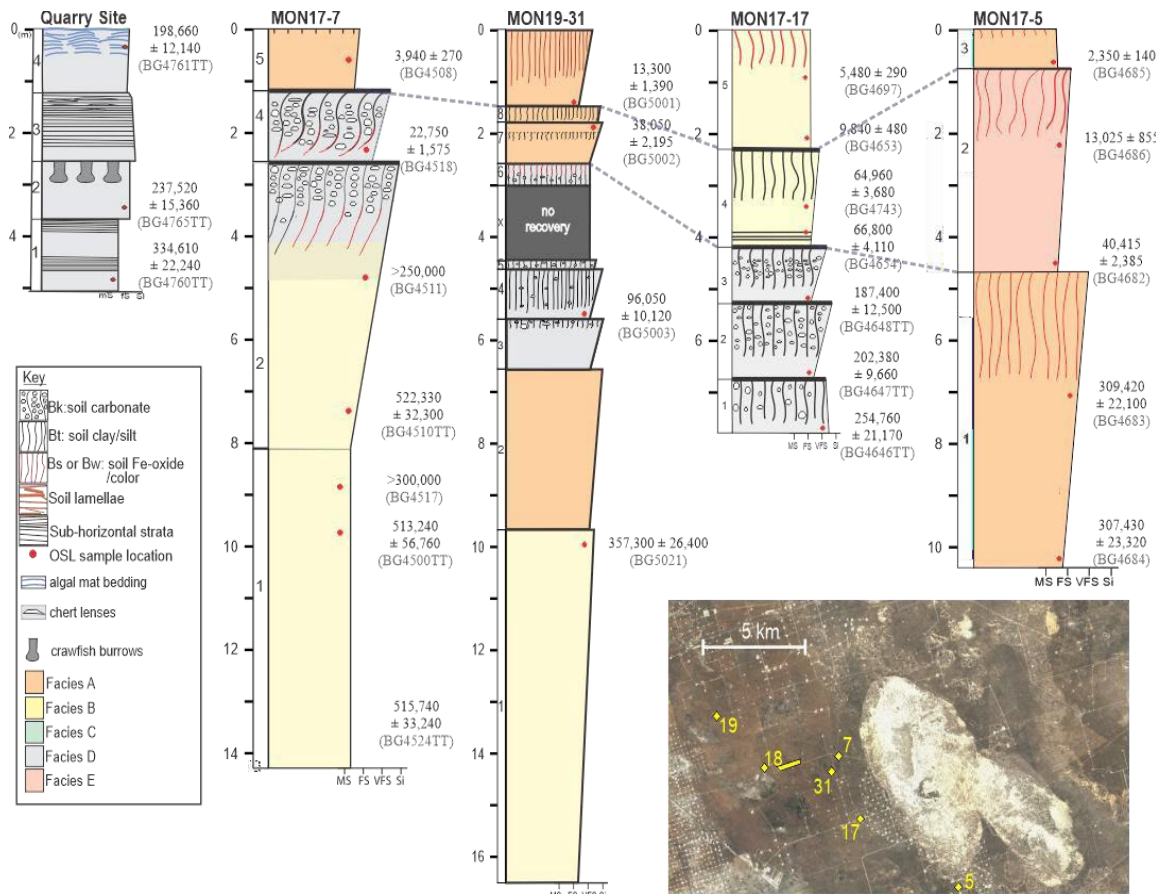


Figure 7. Stratigraphy of geoprobe cores and surface exposure from field area C with locations inset.

(BG4683) that overlap at 1σ while separated by 3 m of massive eolian sand. This field region also included a gravel quarry which exposed 5 m of section. The exposed deposits consisted of indurated carbonate and in places lithified limestone and chert. Four units were observed in this exposure, each characteristic of shallow water carbonate deposition (Wiest et al., 2020). These units were composed primarily of well rounded, likely eolian quartz, carbonate with abundant trace fossils, and evaporitic salt (Wiest et al., 2020). Unit 1 exposed at the base of the section is a poorly consolidated peloidal carbonate with approximately 30% sand and abundant rhizoliths. This basal unit has a TTOSL age of $334,610 \pm 22,240$ (Fig. 7). The nearest sonic boring is AT2-17-10 located 0.8 km northwest of the exposed section. The total thickness of indurated carbonate recorded in this borehole is 9.75 m suggesting the quarry exposes approximately half of the palustrine sequence. The indurated carbonate observed in the quarry was also observed at sites MON18-18 and MON18-19 where the presence of hard carbonate material at the surface inhibited coring.

3D Modeling of Monahans Subsurface Geometry

The three data source: Sonic Borings, Geoprobe cores, and limited geophysical surveys were used to create a 3D model of the subsurface geometry of the Monahans dune field. The model interpolates amongst the stratigraphic information provided by these three data sources (Fig. 8). The complex depositional and pedogenic history of the Monahans was simplified in to four broad stratigraphic units to facilitate modeling: 1) The gravelly, red alluvial clay found at the base of many sonic boreholes, 2) The indurated palustrine carbonates of the playa lake sequence observed in the quarry and

borings, and 3) The eolian sand-rich part of the Blackwater Draw Formation eolian deposits 4) Prominent occurrences of Facies D with stage II-IV of pedogenic carbonate.

An elevation model of the basal the red-clay surface, at the base of the Blackwater Draw Formation (Figs. 9 and 10) reveals a

complex paleotopography. There is a pronounced slope with > 50 m relief from the

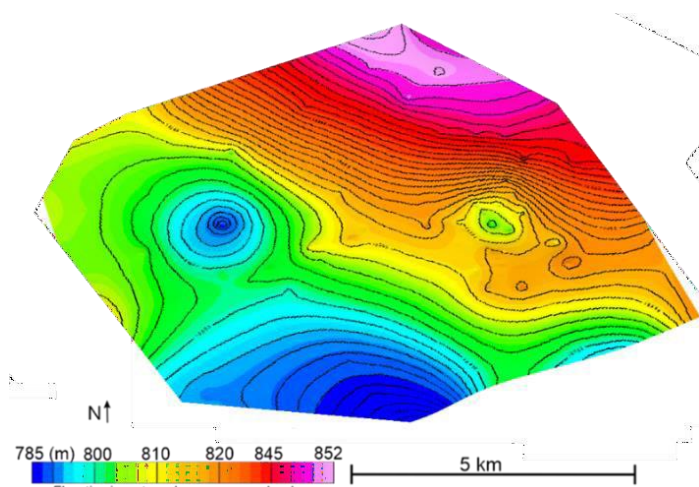


Figure 9. Elevation model of the basal alluvium, in which the Blackwater Draw rests on with color graded contours in meters above mean sea level.

figure is the southwesterly slope of the basal alluvium, the depressions in this surface in both areas A and C, and the distribution of Facies D carbonate soils in regions B and C.

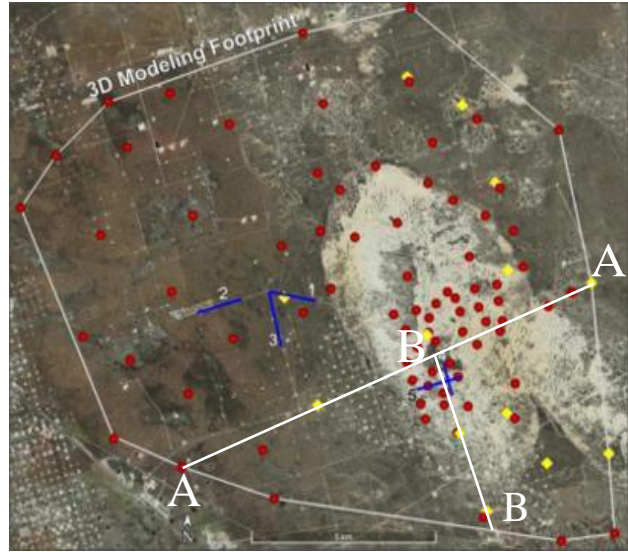


Figure 8. Extent of 3D modeling with data sources: sonic borings (red), geoprobe cores (yellow), geophysical survey lines (blue).

northeast to southwest. Also, there appears to be three distinct circular-like depressions 5-10 m deep. The eastern-most depression is well defined by intensive boreholes and is the mining area for sand. These depressions, and the subsurface topographic relief between the field areas is apparent in cross section A-A' (Figs. 10 and 11). Visible in this

The model also supports field observations at sites MON18-18 and MON18-19 of indurated carbonate at or near the surface. The alluvium is found in the base boreholes, however the lack of sample

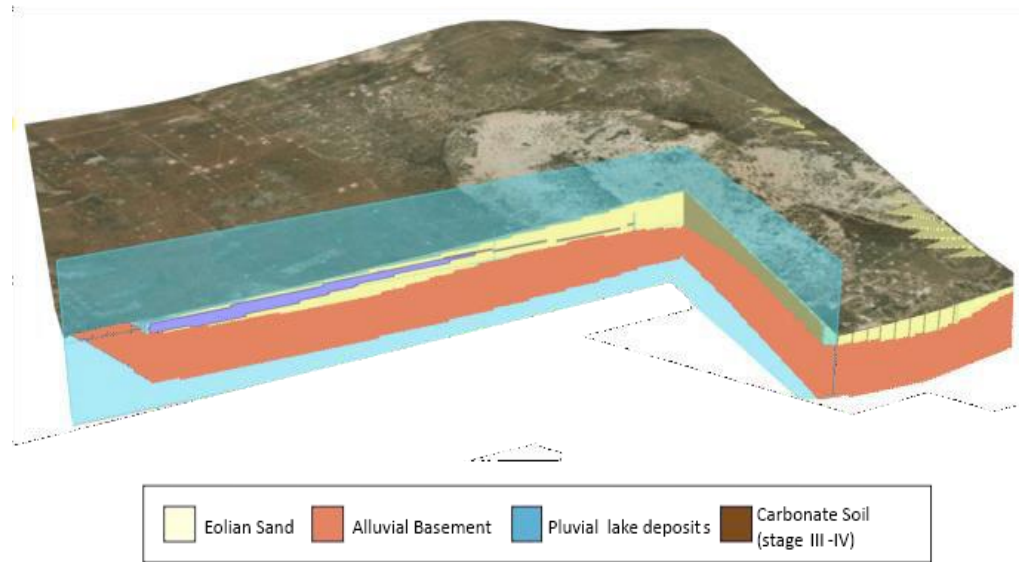


Figure 10. Schematic cross section ABB' of the Monahans dune field. The modeled pluvial lake and carbonate soil deposits represent a minimum extent.

of the recovery from this unit limits chronologic constraint. This strata was described broadly as the Tertiary and Quaternary Pecos Alluvium and is part of the Cenozoic Pecos Alluvium Aquifer (White, 1971, Jones, 2001) In the Monahans area these units dip southwest and are associated with infilling of the Monument Draw Trough of the Dockum group (Muhs and Holliday, 2001, White, 1971, Jones, 2001). The eolian sands of the BWD infill depressions in this alluvial surface beginning prior to 550 ka (BG4997TT). The accumulation and reworking of the BWD eolian sands to form Holocene sand sheet and dunes continues presently. In numerous (16) intervening periods of landscape stability and wetter conditions as indicated by the presence of stage III-IV

carbonate soils and a nearby palustrine sequence. The modeled extent of these soils is a minimum result limited by the density of sampling. These shallow lake deposits rest on eolian sands that which yielded an OSL age of $334,610 \pm 22,240$ yr (BG4760TT). The stromatolite deposits at the top of this shallow water sequence gave an OSL age of $198,660 \pm 12,140$ yr (BG4761TT). Proximal geoprobe cores date the overlying rubified,

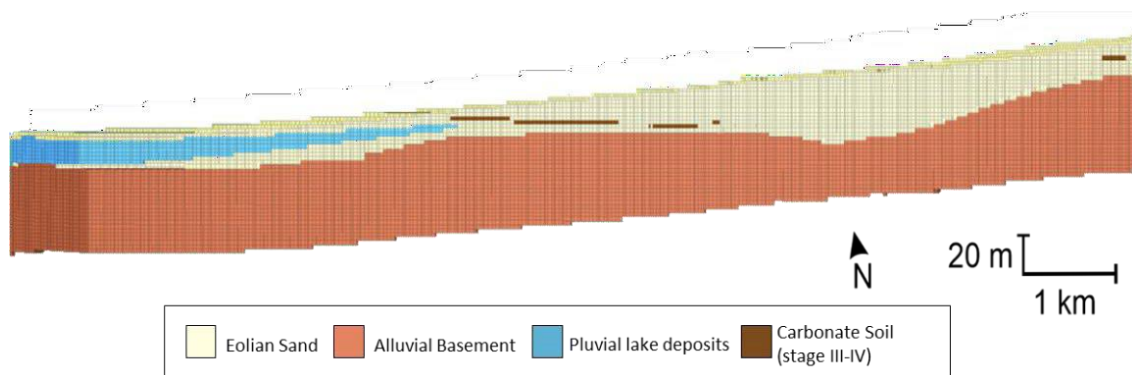


Figure 11. Cross section A-A' of Monahans subsurface deposition presented with 20x vertical exaggeration. Location of cross section shown in Fig. 6.

massive sands to $132,430 \pm 8,860$ yr (BG4993), yielding a minimum limiting age on succession of this lake phase. Near the hypothesized lake margin, it appears that carbonate soil horizons may intercalated with the palustrine deposits, though carbonate paleosols are common in the stratigraphic sequence above and below the palustrine horizon. Core MON19-3 in field are B contains the oldest dated carbonate at $464,530 \pm 29,810$ (BG4563TT) and the youngest found in region C at $22,750 \pm 1,575$ (BG4518). The broad span of carbonate soil formation demonstrates not a single depositional episode, but the complex process of soil formation during multiple periods of humid stability through the late Quaternary. Throughout the formation of these two carbonate rich units, the eolian sand remains constant on the landscape, and supersedes them at the

surface. At the surface, the antecedent southwesterly slope and localized depressions are not reflected. Instead, a topographic inversion of the subsurface topography occurs with infilling by the thickest sands in the eastern depression and the thinnest over the topographic high in the northeast corner of the study area (Fig. 11).

CHAPTER FOUR

Discussion

The combination of the deep reconnaissance borings and detailed study of shallower Geoprobe cores from the Monahans dune field yields new insights in to late Quaternary eolian deposition in the Pecos River basin. A paleo-DEM for the top of the Cenozoic Pecos Alluvium aquifer yields a reconstruction of the antecedent topography that was infilled with Pleistocene and Holocene eolian depositions and paleosols. The sonic borings revealed initial deposition of Blackwater Draw Formation that infilled against the slope and in subsurface depressions and thins eastward to the caprock escarpment (Figs. 9 and 11). Geoprobe cores that sample the upper 30 to 50% of the stratigraphic sequence reveal the pedosedimentary depositional sequence spanning the past ~520 ka. A quarry exposure, borings and Geoprobe cores document pluvial lake deposits that appears intercalated with eolian sand deposition ca. 200 to 250 ka ago.

The oldest strata recorded in this study is the upper surface of the Cenozoic Pecos Alluvium Aquifer. The sonic borings often terminated at this red, weathered, clayey gravel, penetrating this deposit by no more than 2 m. The boring methods prevented undisturbed sample recovery and thus dating. However, these borings are instrumental in defining the subsurface topography of the antecedent pre-Pleistocene surface, onto which the BWD Formation infilled. The general southwest dip of these deposits follows the dip of the Monument Draw Trough (Jones, 2001). Aside from this general dip, the concentration of borings and targeted geophysical survey-lines reveal localized depressions in the sub-surface (Figs. 10 and 11). These closed depressions likely reflect

the salt dissolution features abundant in either the Dockum Group or deeper underlying strata. These depressions are found underlying both the palustrine lake, and the thickest body of eolian sand (Fig. 11) and may have influenced overlying water tables and loci for deposition. These localized depressions and paleo-slope are not reflected in the present topography overlying the alluvial basement is the eolian BWD. Previously, the BWD has an inferred Pliocene to Pleistocene age of ca. 1.6 ka, with the Guaje ash providing the sole chronologic control of >1.61 ma (Holiday, 1989, Gustavson and Holliday, 1999, Izett and Obradovich, 1994). In this study the deepest eolian sand recovered yielded finite ages of ~550 ka (BG4997TT). The chronostratigraphy of Monahans dune field deposits (Fig. 12) reveal a recurring sequence of deposition of eolian sand followed by pedogenesis and erosion until conditions again facilitate eolian reactivation. Each of these observed sequences has been designated an eolian depositional phase (EDP). The oldest identified eolian depositional phase (EDP 1) yielded TT-OSL ages between ca. 555 and 513 ka, which is capped by cambic paleosol in three localities. Unconformably overlying this paleosol is EDP 2 which is characterized by aeolian sedimentary unit dominated by a calcic paleosol, with one age of ca. 465 ka. The third phase is constrained by two ages at ca. 380 and 357 ka at its upper bound. This phase is observed in cores 8 and 31 from the sand sheet east and west of the active dunes and includes up to 7 m of eolian sand. The weakly developed Bwb soils that cap EDP 3 is followed by the only eolian deposits observed in both outcrop and cores. Phase 4 was deposited between ca. 335 and 308 ka with the older deposition observed in the quarry and two penecontemporary units in BWD sediments to the southeast. The oldest age of EDP 5 of ~287 ka is also the oldest

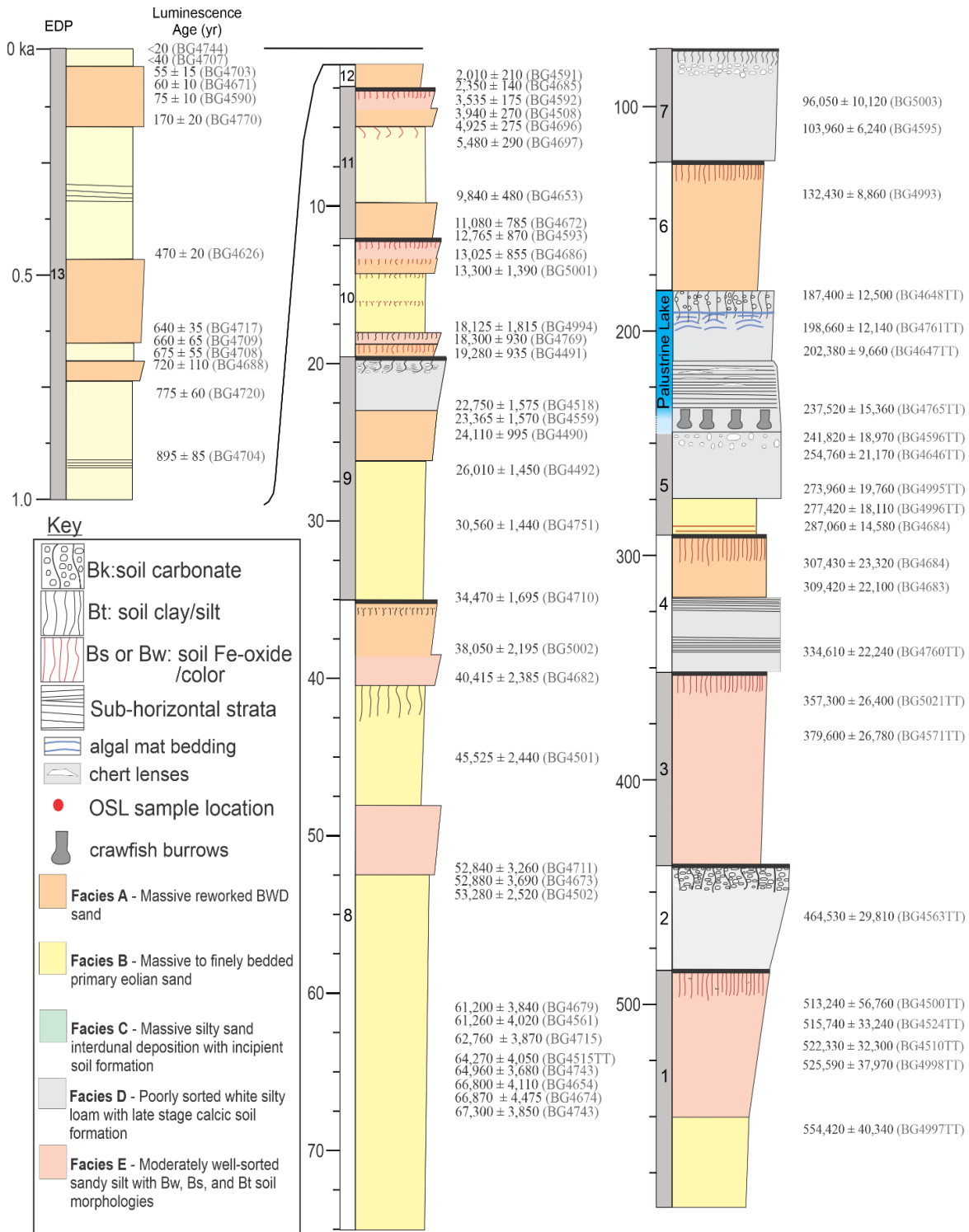


Figure 12. Composite chronology of the Monahans Dune Field. Depicted are eolian depositional phases (numbered 1-13), pluvial deposition (blue), primary facies encountered in geoprobe cores, and luminescence ages of eolian deposits.

age recorded in a core taken on the active modern dunes. The upper most aeolian sediment for Phase 5 is the ca. 241 ka age from aeolian sand beneath the palustrine complex. The pluvial deposit that overlies EDP 5 includes ~5 m of subaqueous carbonate deposits. This deposit extends from ca. 238 to 190 ka where it is capped by coeval bioassisted shallow water carbonate, and proximal pedogenic carbonate deposits in geoprobe core 7. EDP 6 unconformably overlies the lake deposits and is constrained by a single age of ca. 132 ka. EDP 7 is found in two geoprobe cores and includes poorly sorted material dated to ca. 100 ka. The compound well-developed soils that cap EDP 7 are followed by the second thickest body of primary eolian sand observed in geoprobe cores. EDP 8 includes concentration of ages at between 67 and 61 ka, ca. 52 ka, a single age at 45 ka, and ca. 40 ka. These deposits are up to 5 m thick and signify a profound period of eolian accumulation. EDP 9 extends from ca. 34 to 23 ka this phase is dominated by massive sands and is the most recent phase to include carbonate soil morphologies. EDP 10 is observed in 4 geoprobe cores and is characterized by more poorly sorted material and multiple weakly developed paleosols. EDP 11 records the first Holocene deposition in the Monahans with a maximum age of ca 12 ka and eolian deposition free of major hiatuses through 3.5 ka. A final thin accumulation >1 ka is observed in two cores at ca. 2.3 to 2 ka. to form the penultimate EDP 12. The most recent EDP is constrained by a basal age of 895 ± 85 years and is characterized by massive to finely bedded primary eolian sand with no evidence of pedogenic alteration or hiatus from then through a series of four ages in the past century.

A finite mixture model analysis of recorded ages >1 ka yielded 11 components as defined within 1 sigma errors (Table 3 and Fig. 13). Each of the identified populations is

indicative of major eolian reactivation. A probability density function (PDF) also demonstrates the statistical significance of observed FMM populations (Fig. 13). The best constrained and most profound eolian reactivations are identified by both the FMM and peaks in probability (Fig. 13 and Table 3).

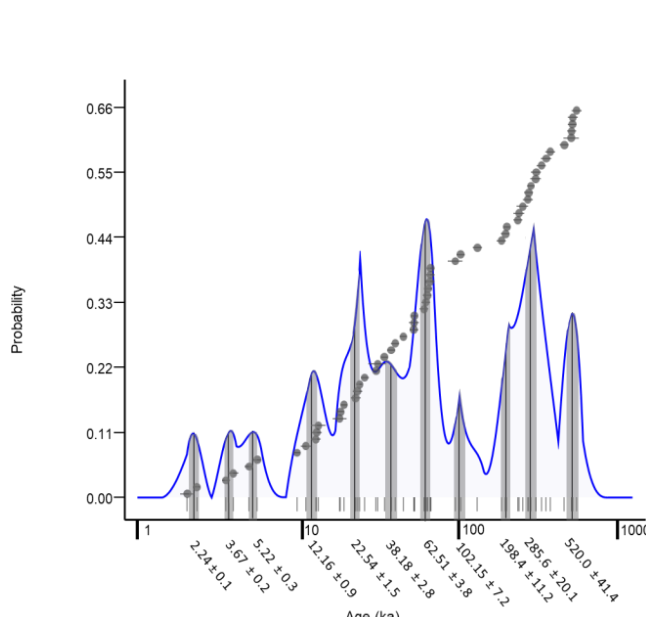


Table 3. Finite mixture model components with associated errors of Monahans dune field luminescence ages. listed in red.

Age (ka)	1 a	ecorunotsr s
520	41.4	6
292.6	20.7	10
196.1	11.1	2
102.1	7.2	3
62.5	3.8	10
38.2	2.8	6
22.5	1.5	7
12.2	0.9	5
5.2	0.3	2
3.7	0.2	2
2.2	0.1	2

Figure 13. Distribution of Monahans Luminescence Ages. This figure plots both a probability density function (PDF) of all ages collected >1ka (blue) as well as the 11 populations (black line with associated errors in grey) identified by a finite mixture model (FMM). Each of the ages (n=57) is represented by a grey hash

Periods of erosion and dune accumulation however are dominant, with dense populations of osl ages associated with the most pronounced of these episodes (Fig. 113 and Table 3). A finite mixture model analysis of recorded ages >1 ka yielded 11 components (Fig. 13 and Table 3). Seven of these components were defined by more than five ages. While those with fewer than five defining ages reflect depositional periods, those with more ages are more statistically significant. This significance, along with the errors associated with age define the curve of a probability density function (Figure 13)

which also depicts the eleven FMM component populations. This reactivation is associated with climate forcing. Each of the defined eolian populations appear to coincide during transitional periods in the oxygen isotope derived sea level record associated with northern latitude ice sheet extents (Spratt and Lisiecki, 2016, Lisiecki, 2005, Batchelor 2015). The FMM derived eolian depositional periods did not occur on either maximum or minimum glacial extents. While the conditions for eolian accumulation was modulated by ice sheet extents, each population is recorded at an intermediate condition following. During these periods, the accumulation and southern extension of the Laurentide ice sheet is modeled to have altered of North American circulation and thus the transport of moisture into the Monahans Dunes fields, and the Great Plains as a whole (Bolles and Forman, 2018, Forman et al., 2001, Halfen and Johnson, 2013, Donat et al., 2015).

Conclusions

This study presents stratigraphic, pedosedimentary, and chronologic observations to advance the study of late Quaternary eolian deposition in the Monahans dune system. Data from 81 deep sonic borings and 5 passive seismic transects were employed to create a 3D visualization of the surface of Cenozoic Pecos Alluvium deposits upon which BWD eolian sediments accumulated. These data, along with geoprobe cores and a surface exposure record a palustrine lake sequence. Finite age constraints on this MOIS 7 aqueous system was provided by use of OSL and TT-OSL dating under SAR protocols. Luminescence dating of in-tact sediment cores documents 13 identified eolian depositional phases in the region since ~554 ka. OSL and TT-OSL data supplement the

existing record of luminescence and radiocarbon ages which were limited to strata exposed at or near the surface.

This chronostratigraphic analysis indicates the initiation of eolian deposition at climate transitions. One well documented period of dune accretion is from glacial to interglacials for the late Pleistocene through the Holocene, ca. 23 to 3 ka. In turn, there was pronounced eolian deposition from the transition from the last interglacial (*sensu lato*) ca. 70 ka to 45 ka with glacial like conditions. There are older periods of eolian deposition at ca. 287 to 250 ka, 380 to 335 ka, and 525 to 513 ka. A shallow playa-like lake formed adjacent to the Monahans dune field ca. 240-200 ka and episodes of pedogenesis are mostly confined during glacials, with ice sheet induced southern displacement of a merged subtropical-polar jet streams (e.g., Benson et al., 2003; Oviatt et al., 2003; Adams et al., 2008; Patrickson et al., 2010; Schmidt, 2011; Nelson and Jewell, 2015; Thompson et al., 2016; McGee, 2020).

This study follows work across the Great Plains which hypothesize a correlation between eolian reactivation events and climate forcing. The high-resolution stratigraphy and chronology collected through this study build towards extending this work into the Monahans Dune System. The data presented here represents the groundwork for future studies of chronology, hydrology, and stratigraphy in the Monahans which aim to improve our understanding of the system and develop the Monahans depositional record into a robust paleoclimate proxy record for the late Quaternary in the Southern High Plains.

APPENDIX

Appendix A

Figures and Tables

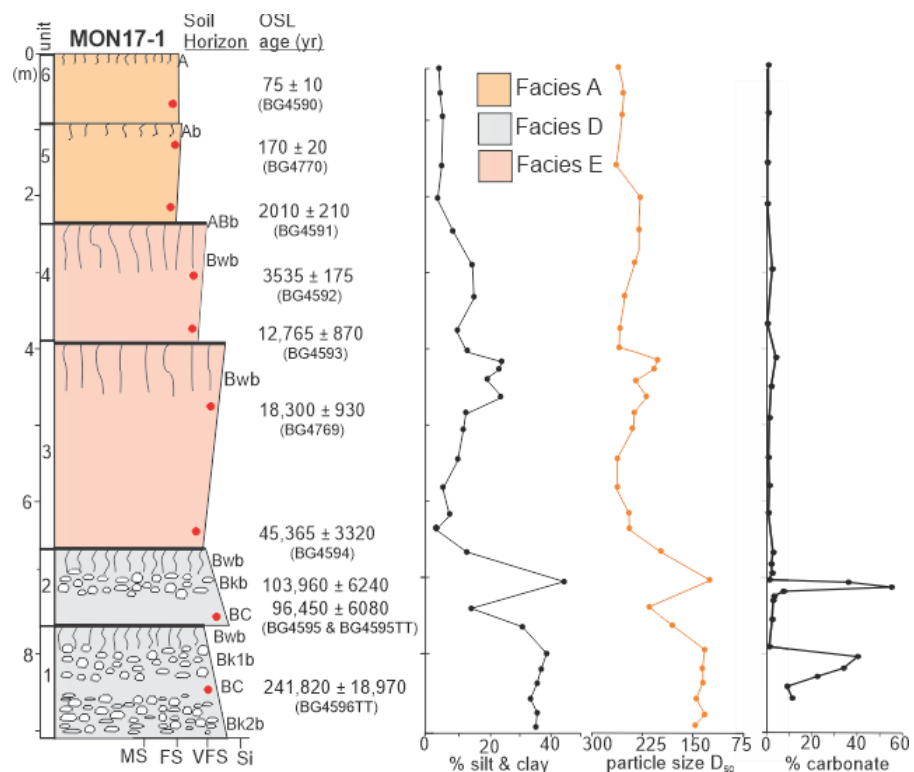


Figure A.1. Stratigraphy of geoprobe core MON17-1

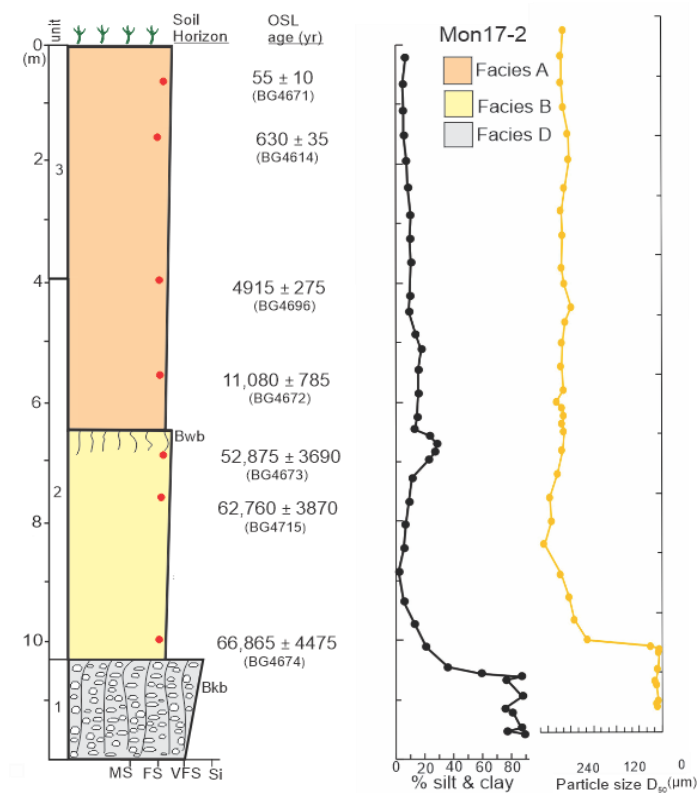


Figure A.2. Stratigraphy of geoprobe core MON17-2

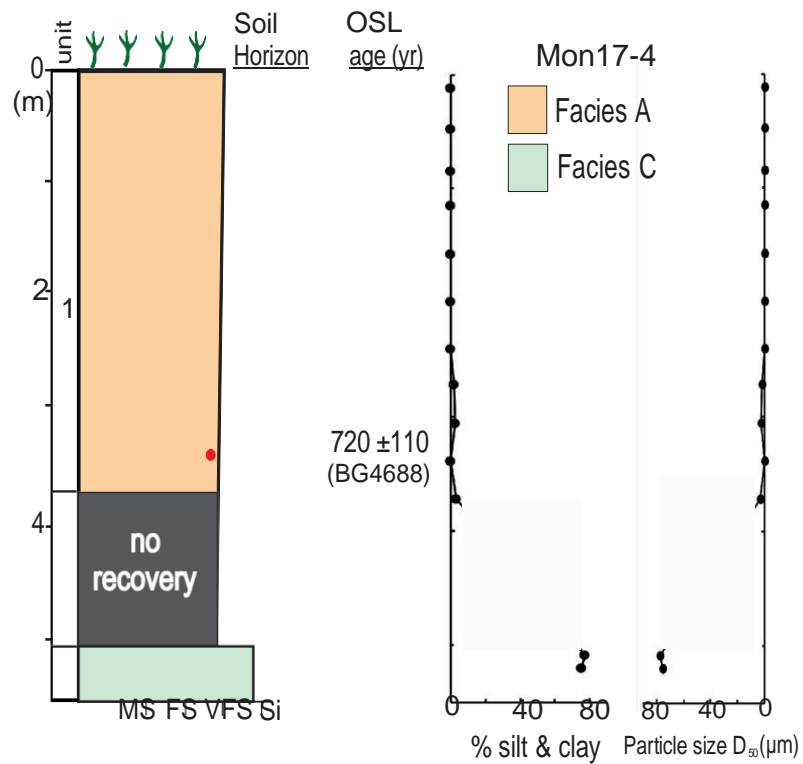


Figure A.4. Stratigraphy of geoprobe core MON17-4

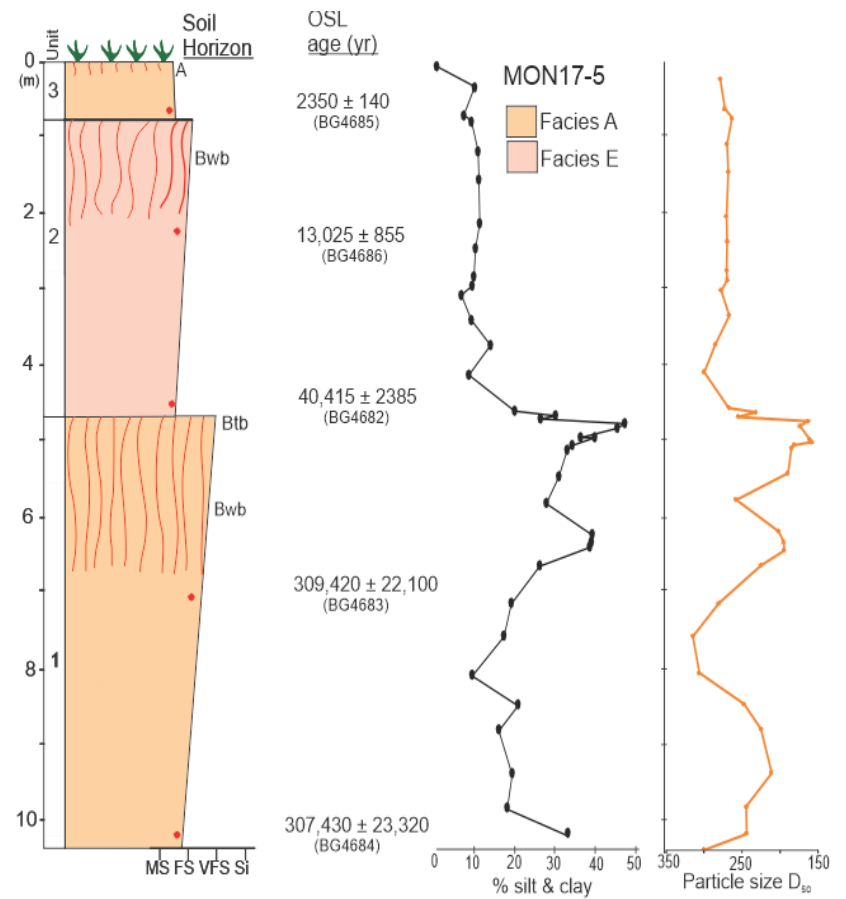


Figure A.5. Stratigraphy of geoprobe core MON17-5

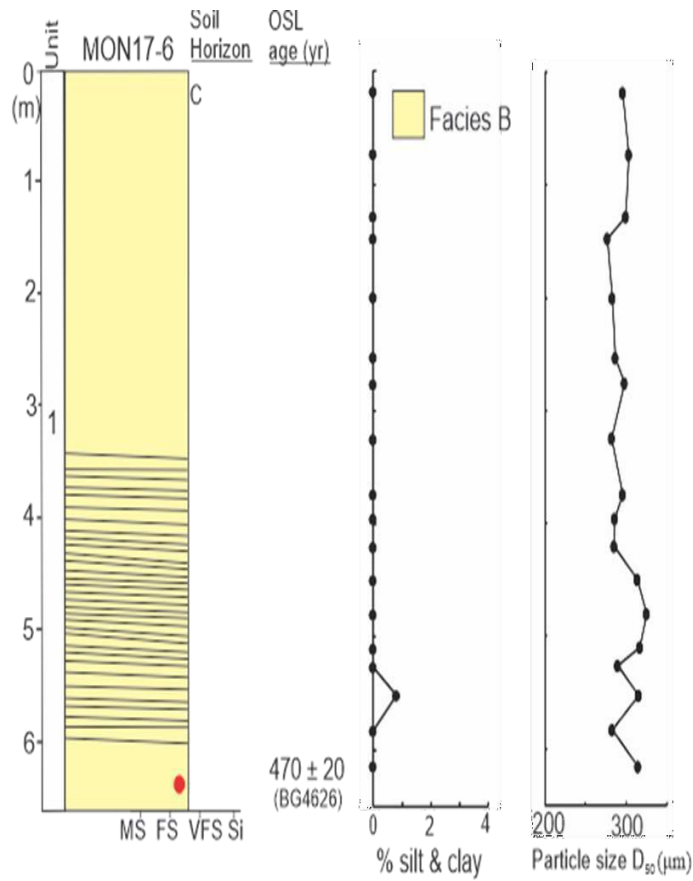


Figure A.5. Stratigraphy of geoprobe core MON17-6

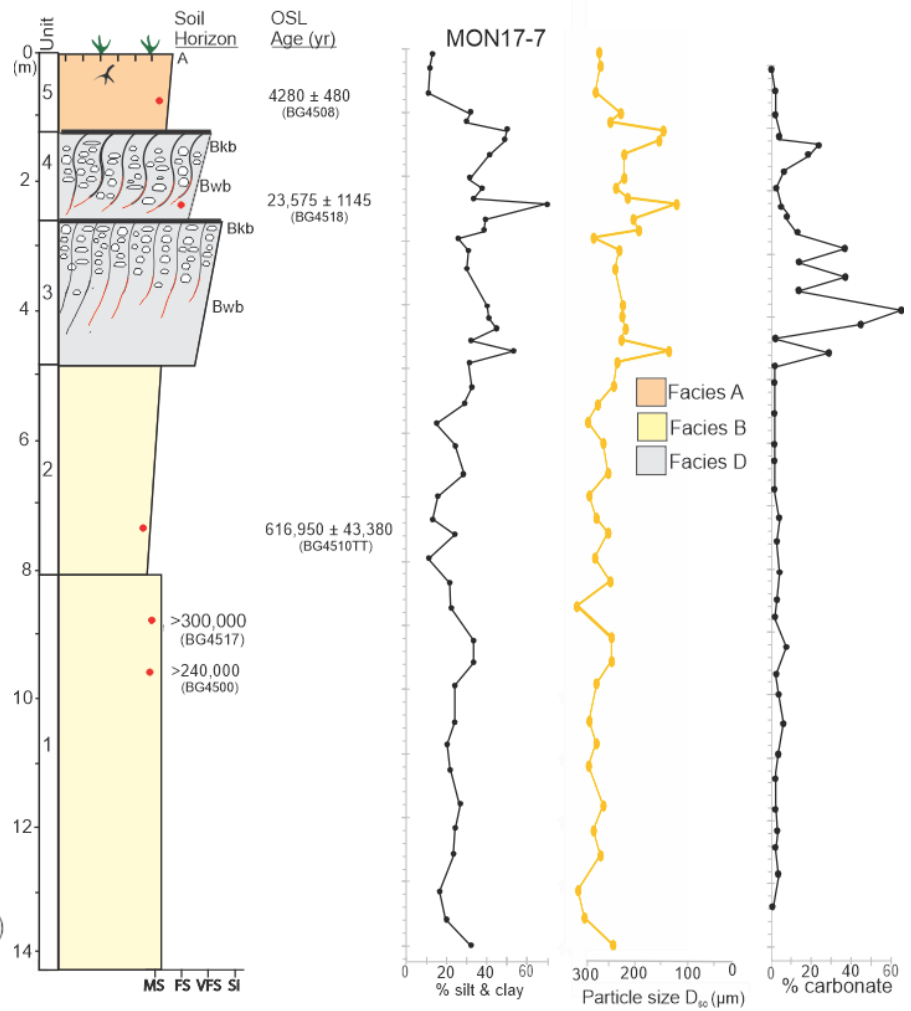


Figure A.6. Stratigraphy of geoprobe core MON17-7

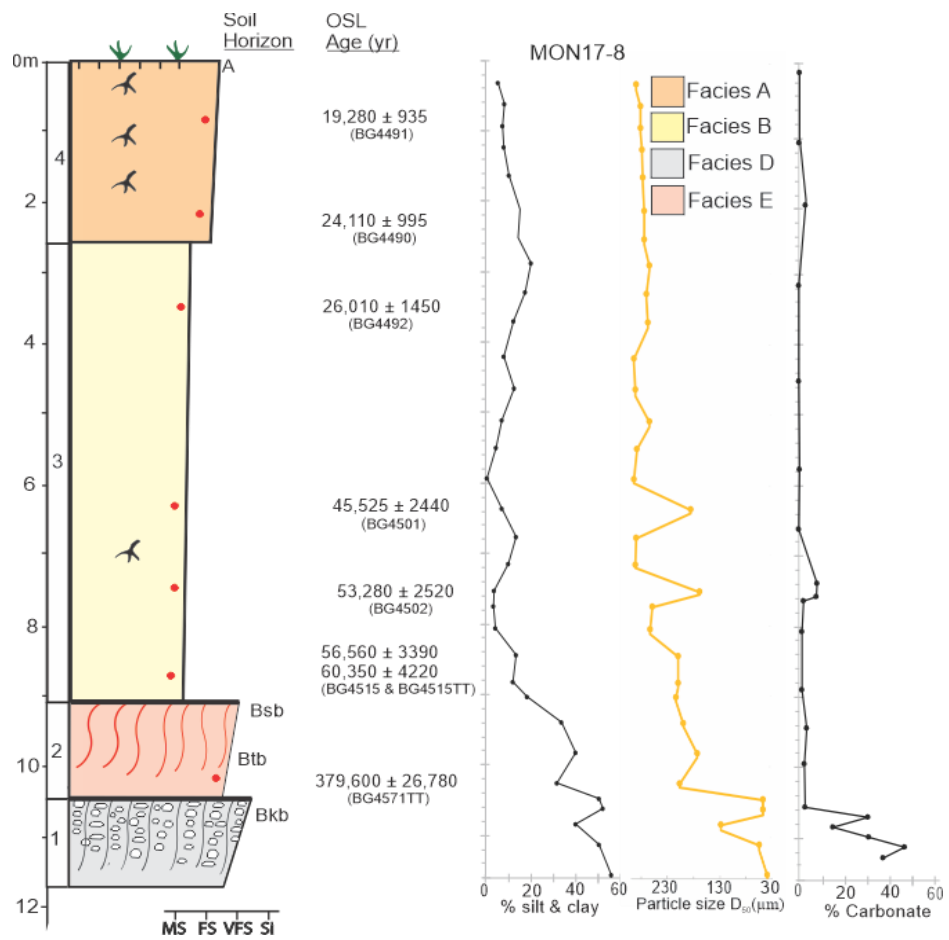


Figure A.7. Stratigraphy of geoprobe core MON17-8

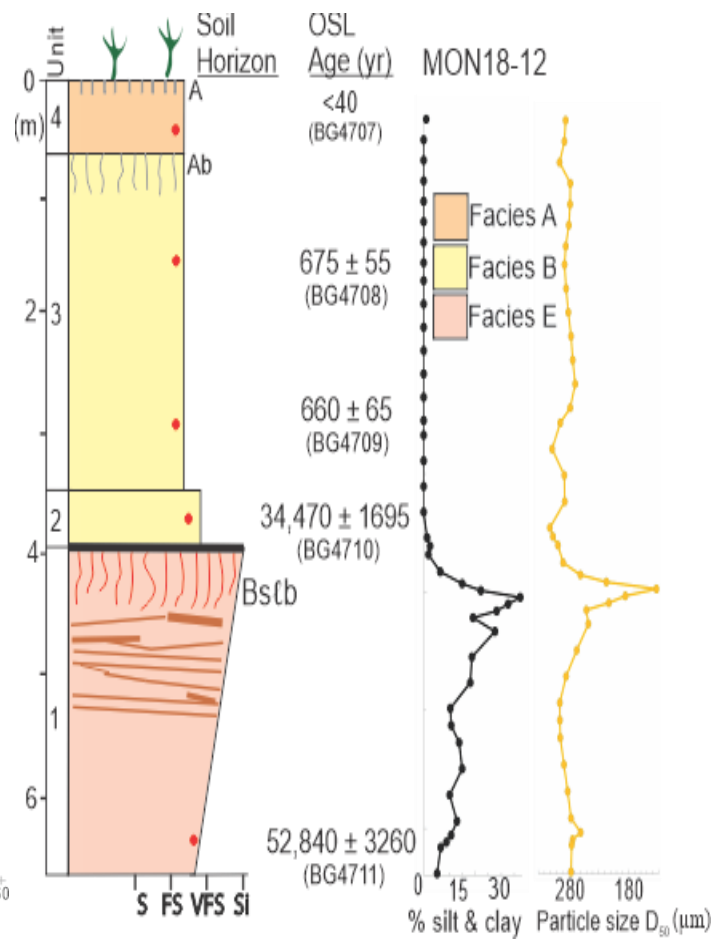


Figure A.8. Stratigraphy of geoprobe core MON18-12

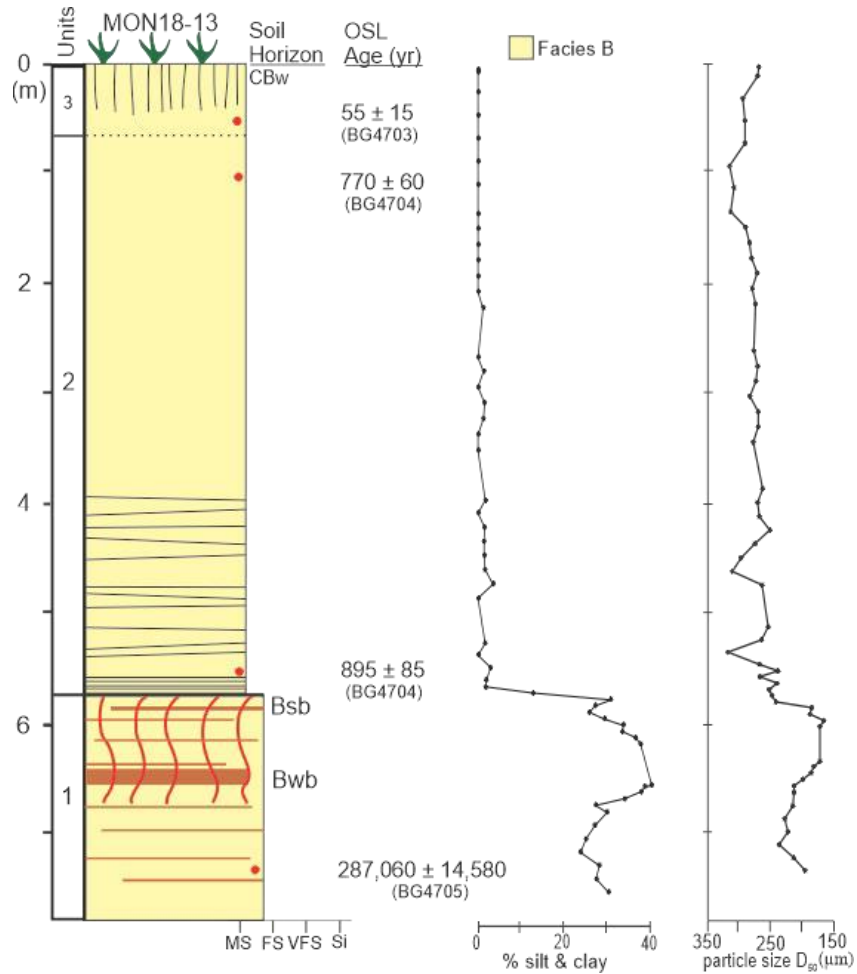


Figure A.9. Stratigraphy of geoprobe core MON18-13

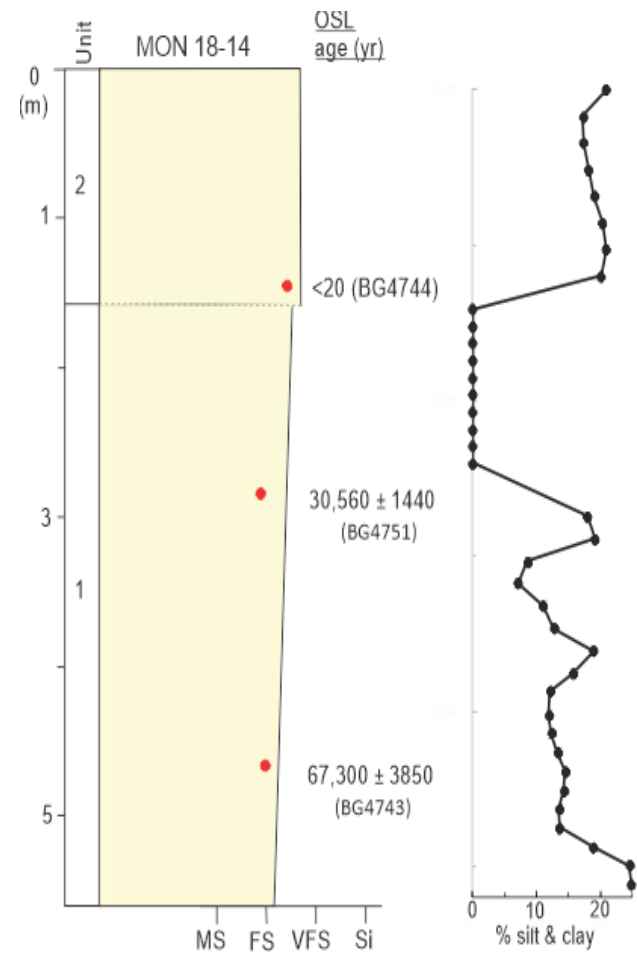


Figure A.10. Stratigraphy of geoprobe core MON18-14

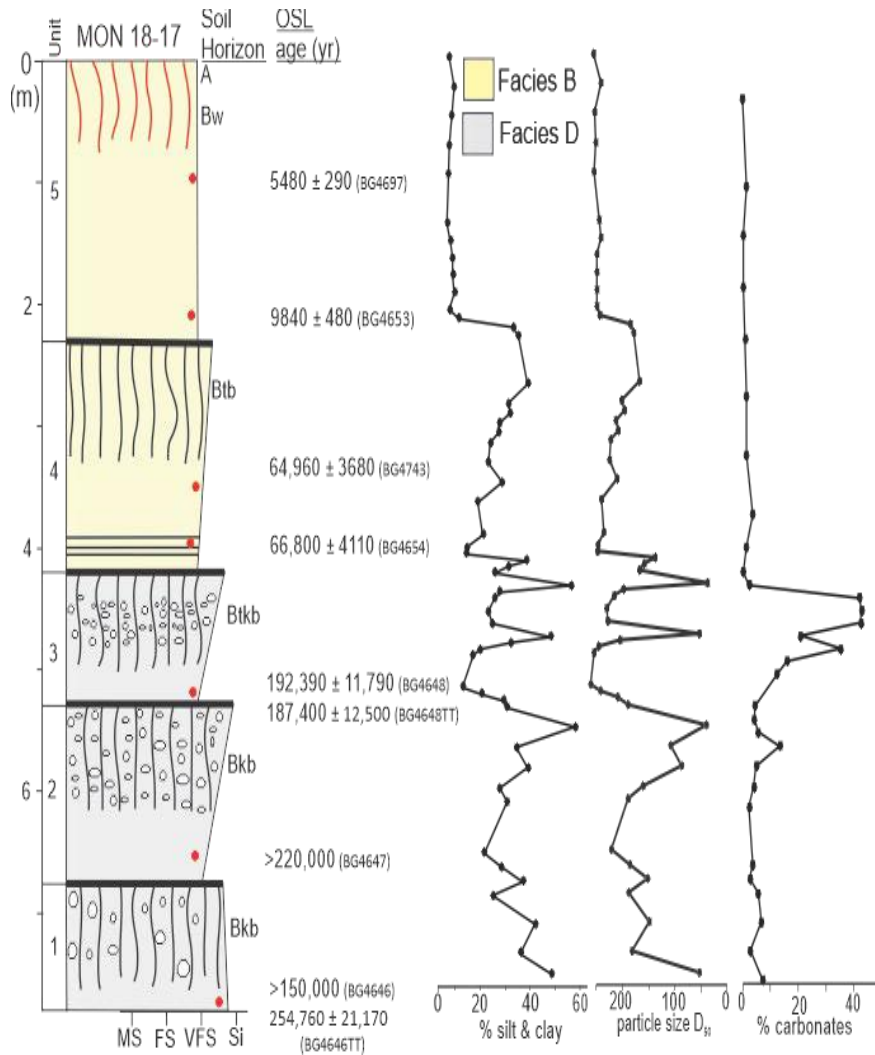


Figure A.11. Stratigraphy of geoprobe core MON18-17

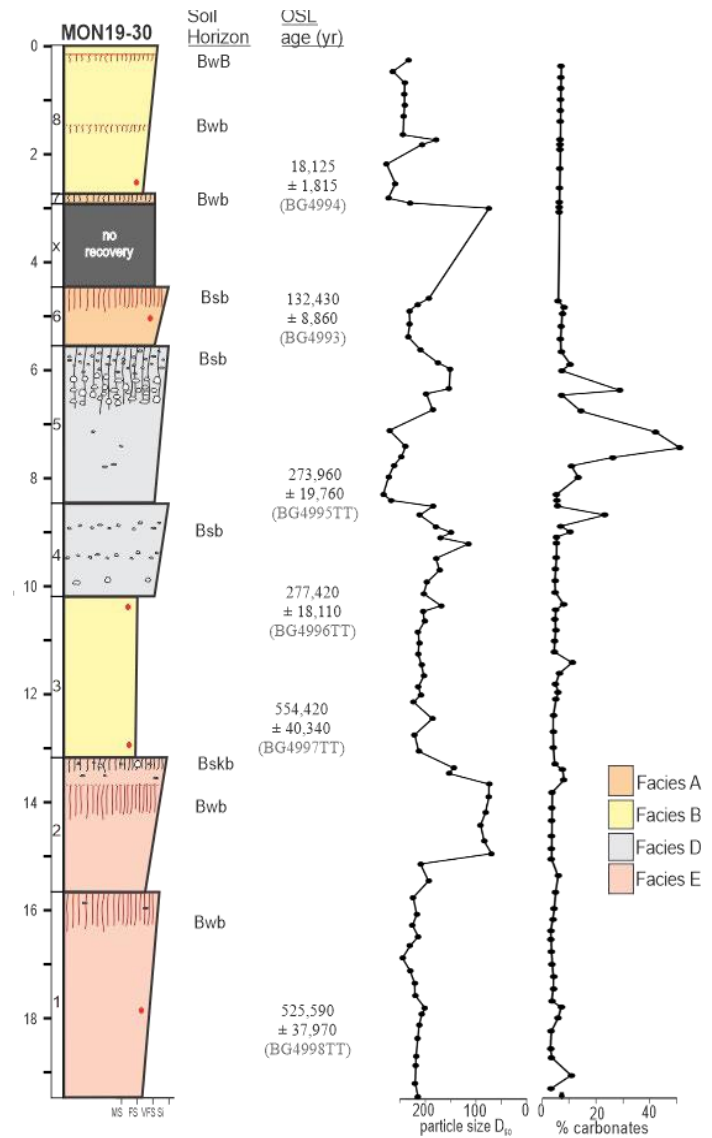


Figure A.12. Stratigraphy of geoprobe core MON18-30

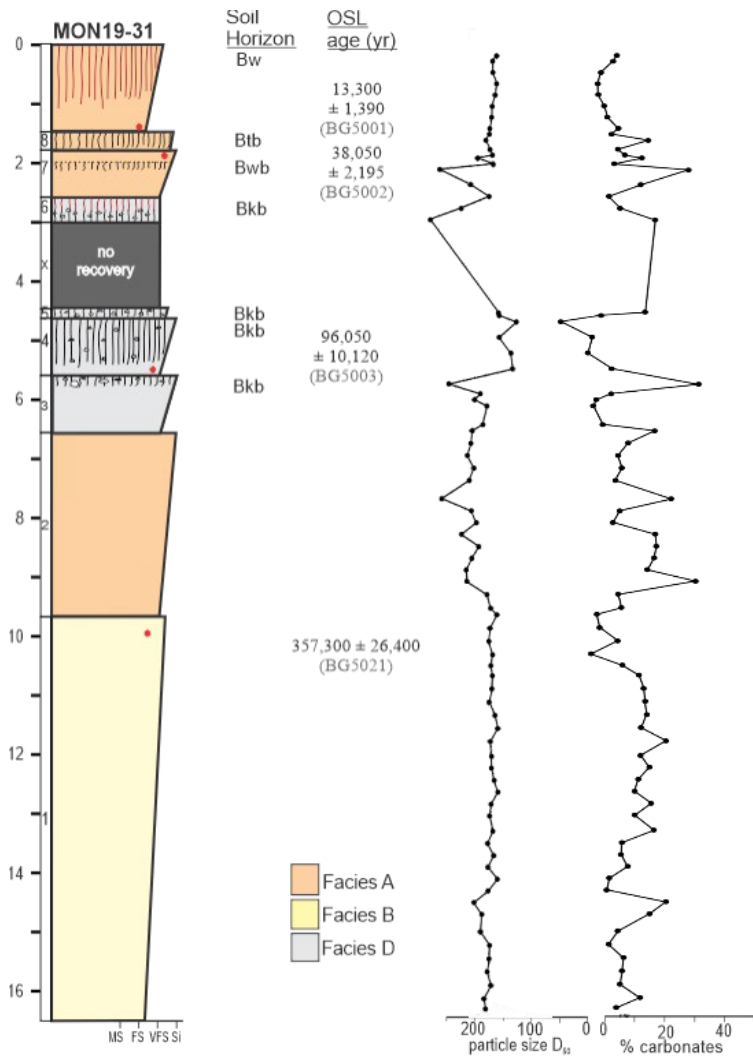


Figure A.13. Stratigraphy of geoprobe core MON19-31

REFERENCES

- Adamiec, G., Duller, G.A.T., Roberts, H.M., Wintle, A.G. (2010). Improving the TT-OSL SAR protocol through source trap characterization: *Radiat. Meas.*, 45(7), 768-777
- Adams, K.D., Goebel, T., Graf, K., Smith, G.M., Camp, A.J., Briggs, R.W., Rhode, D. (2008). Late Pleistocene and early Holocene lake-level fluctuations in the Lahontan basin, Nevada: Implications for the distribution of archaeological sites, *Geoarchaeology*, 5, 608-643.
- Anderson, R. Y., Allen, B. D., and Menking, K. M., 2002, Geomorphic expression of abrupt climate change in southwestern North America at the glacial termination: *Quaternary Research*, v. 57, no. 3, p. 371-381.
- Aitken, M. J., 1998. An introduction to optical dating: the dating of Quaternary sediments by the use of photon-stimulated luminescence. Oxford; New York, Oxford University Press.
- Aitken, M.J. (1985). *Thermoluminescence Dating*. London Academic Press, 247.
- Arnold, L.J., Demuro, M., Parés, J.M., Arsuaga, J.L., Aranburu, A., Bermúdez de Castro, J.M., Carbonell, E. (2014). Luminescence dating and palaeomagnetic age constraint on hominins from Sima de los Huesos, Atapuerca, Spain. *J. Hum. Evol.* 67, 85–107.
- Arnold, L.J., Demuro, M., Pares, J.M., Perez-Gonzalez, A., Arsuaga, J.L., de Castro, J. M.B., and Carbonell, E., (2015), Evaluating the suitability of extended-range luminescence dating techniques over early and Middle Pleistocene timescales: Published datasets and case studies from Atapuerca, Spain: *Quat. International*, 389, 167-190.
- Arnold, L.J., Demuro, M., Spooner, N.A., Prideaux, G.J., McDowell, M.C., Camens, A.B., Reed, E.H., Pares, J.M., Arsuaga, J.L., de Castro, J.M.B., Carbonell, E. (2018). Single-grain TT-OSL bleaching characteristics: Insights from modern analogues and OSL dating comparisons: *Quat. Geochronol.*, 49, 45-51.
- Athanassas, C., Zacharias, N. (2010). Recuperated-OSL dating of quartz from Aegean (South Greece) raised Pleistocene marine sediments: current results. *Quat. Geochronol.* 5, 65–75.
- Batchelor, C.L., Margold, M., Krapp, M., Murton, D.K., Dalton, A.S., Gibbard, P.L., Stokes, C.R., Murton, J.B., Manica, A. (2019). The configuration of Northern Hemisphere ice sheets through the Quaternary: *Nature Communications*, 10 (3713).

- Bartz, M., Arnold, L.J., Demuro, M., Duval, M., King, G.E., Rixhon, G., Posada, C.A., Pares, J. M., Bruckner, H. (2019). Single-grain TT-OSL dating results confirm an Early Pleistocene age for the lower Moulouya River deposits (NE Morocco): *Quat. Geochronol.*, 49, 138-145.
- Benson, L., Lund, S., Negrini, R., Linsley, B., Mladen, Z. (2003). Response of North American Great Basin Lakes to Dansgaard-Oeschger oscillations: *Quat. Sci. Revs*, 22(21-22), 2239-2251.
- Bolles, K. C. and S. L. Forman (2018). "Evaluating Landscape Degradation Along Climatic Gradients During the 1930s Dust Bowl Drought From Panchromatic Historical Aerial Photographs, United States Great Plains." *Frontiers in Earth Science*.
- Bøtter-Jensen, L., Andersen, C.E., Duller, G.A.T., Murray, A.S., 2003. Developments in radiation, stimulation, and observation facilities in luminescence measurements. *Radiation Measurements* 37, 535-541.
- Boulila, S., Galbrun, B., Miller K.G., Pekar, S.F., Browning, J.V., Laskar, J., Wright, J.D. (2011). On the origin of Cenozoic and Mesozoic "third-order" eustatic sequences: *Earth Sci Rev* 109:94–112
- Blakey, R.C., Ranney, W.D. (2018). *Changing Tectonics, Cooling Climates and the Dawn of Crustal Extension: Late Eocene to Early Miocene (ca. 35-20 Ma) Ancient Landscapes of Western North America*: Springer.
- Broecker, W. S., Mcgee, D., Adams, K. D., Cheng, H., Edwards, R. L., Oviatt, C. G., and Quade, J., 2009, A Great Basin-wide dry episode during the first half of the Mystery Interval?: *Quaternary Science Reviews*, v. 28, no. 25-26, p. 2557-2563.
- Brown, N.D., Forman, S.L. (2012). Evaluating a SAR TT-OSL protocol for dating fine-grained quartz within Late Pleistocene loess deposits in the Missouri and Mississippi river valleys, United States: *Quat. Geochronol.*, 12, 87-97.
- Carlisle, W.J., Marrs, R.W. (1982). Eolian features of the Southern High Plains and their relationship to windflow patterns, in Marrs, R.W., and Kolm, K.E., eds., *Interpretation of windflow characteristics from eolian landforms*: GSA Special Paper, 192, 89-105.
- Chandler, V. W. and R. S. Lively., 2016. Utility of the horizontal-to-vertical spectral ratio passive seismic method for estimating thickness of Quaternary sediments in Minnesota and adjacent parts of Wisconsin. *Interpretation-a Journal of Subsurface Characterization* 4(3): Sh71-Sh90.
- Clarke, M. L., and Rendell, H. M., 2003, Late Holocene dune accretion and episodes of persistent drought in the Great Plains of Northeastern Colorado: *Quaternary Science Reviews*, v. 22, no. 10-13, p. 1051-1058.

- Cook, B.I., E.R. Cook, K.J. Anchukaitis, R. Seager, and R.L. Miller, 2011: Forced and unforced variability of twentieth century North American droughts and pluvials. *Clim. Dyn.*, 37, 1097-1110
- Cunningham, A.C., Wallinga, J. (2012). Realizing the potential of fluvial archives using robust OSL chronologies: *Quat. Geochronol.*, 12, 98-106.
- Donat, M. G., et al. (2016). "More extreme precipitation in the world's dry and wet regions." *Nature Climate Change* 6(5): 508
- Duller, Geoff. (2003). Distinguishing quartz and feldspar in single grain luminescence measurements: *Radiat. Meas.*, 37, 161-165. 10.1016/S1350-4487(02)00170-1.
- Duller, G.A.T. (2008). Single-grain optical dating of Quaternary sediments: why aliquot size matters in luminescence dating: *Boreas*, 37(4), 589-612.
- Duller, G.A.T., Wintle, A.G. (2012). Improving the accuracy and precision of equivalent doses determined using the optically stimulated luminescence signal from single grains of quartz: *Radiat. Meas.*, 47(9), 770-777.
- Duller, G.A.T. (2015). The Analyst software package for luminescence data: overview and recent improvements: *Ancient TL*, 33, 35-42.
- Durcan, J. A., Duller, G.A.T. (2011). The fast ratio: A rapid measure for testing the dominance of the fast component in the initial OSL signal from quartz: *Radiat. Meas.*, 46(10), 1065-1072.
- Eyles, N. (1993). Earths Glacial Record and its Tectonic Setting: *Earth-Science Reviews*, 35(1-2), 1-248.
- Faershtein, G., Porat, N., Matmon, A. (2018). Natural saturation of OSL and TT-OSL signals of quartz grains from Nilotic origin. *Quat. Geochronol.*, 49. 10.1016/j.quageo.2018.04.002.
- Fain, J., Soumana, S., Montret, M., Miallier, D., Pilleyre, T., & Sanzelle, S., 1999. Luminescence and ESR dating-Beta-dose attenuation for various grain shapes calculated by a Monte-Carlo method. *Quat. Sci. Rev.* 18, 231-234.
- Forman, S.L. (2015). Episodic eolian sand deposition in the past 4000 years in Cape Cod National Seashore, Massachusetts, USA in response to possible hurricane/storm and anthropogenic disturbances. *Frontiers in Earth Science*, 3.
- Forman, S. L., Nordt, L., Gomez, J., and Pierson, J., 2009, Late Holocene dune migration on the south Texas sand sheet: *Geomorphology*, v. 108, no. 3-4, p. 159-170.
- Forman, S.L., Oglesby, R., Webb, R.S. (2001). Temporal and spatial patterns of Holocene dune activity on the Great Plains of North America: megadroughts and climate links: *Global and Planetary Change*, 29(1-2), 1-29.

- Forman, S.L., Oglesby, R., Markgraf, V., Stafford, T. (1995). Paleoclimatic significance of late quaternary eolian deposition on the Piedmont and High-Plains, Central United-States: *Global and Planetary Change*, 11(1-2), 35-55.
- Forman, S.L., Tripaldi, A., Ciccio, P.L. (2014). Eolian sand sheet deposition in the San Luis paleodune field, western Argentina as an indicator of a semi-arid environment through the Holocene: *Palaeogeogr. Palaeoclimatol. Palaeoecol.*, 411, 122-135.
- Galbraith, R.F., Roberts, R.G. (2012). Statistical aspects of equivalent dose and error calculation and display in OSL dating: An overview and some recommendations. *Quat. Geochronol.* 11, 1-27.
- Geoprobe Systems., 2011. Geoprobe Macro-Core MC5 1.25-inch Light-Weight Center Rod Soil Sampling System. Technical Bulletin. MK3139, 16-17.
- Gile, L.H., Peterson, F.F., Grossman, R.B. (1966). Morphological and Genetic Sequences of Carbonate Accumulation in Desert Soils: *Soil Science*, 101(5), 347
- Gustavson, T. C., 1991, Buried Vertisols in Lacustrine Facies of the Pliocene Fort-Hancock Formation, Hueco Bolson, West Texas and Chihuahua, Mexico: *Geological Society of America Bulletin*, v. 103, no. 4, p. 448-460.
- Gustavson, T.C., Holliday, V.T. (1999). Eolian sedimentation and soil development on a semiarid to subhumid grassland, Tertiary Ogallala and Quaternary Blackwater Draw Formations, Texas and New Mexico High Plains: *Journal of Sedimentary Research*, 69(3), 622-634.
- Halfen, A.F., Johnson, W.C. (2013). A review of Great Plains dune field chronologies: *Eolian Research*, 10, 135-160.
- Hall, S.A. (2001). Geochronology and paleoenvironments of the glacial-age Tahoka Formation, Texas and New Mexico High Plains, *New Mexico Geology*, 23(3), 71-77.
- Hall, S. A., and Goble, R. J., 2008, Archaeological geology of the Mescalero Sands, Southeastern New Mexico: *Plains Anthropologist*, v. 53, no. 207, p. 279-290.
- Hall, S. A., and Goble, R. J., 2015, OSL age and stratigraphy of the Strauss sand sheet in New Mexico, USA: *Geomorphology*, v. 241, p. 42-54.
- Hall, S. A., Miller, M. R., and Goble, R. J., 2010, Geochronology of the Bolson sand sheet, New Mexico and Texas, and its archaeological significance: *Geological Society of America Bulletin*, v. 122, no. 11-12, p. 1950-1967.
- Hall, S. A., Miller, M. R., and Goble, R. J., 2012, Geochronology and stratigraphy of the Bolson sand sheet: Reply: *Geological Society of America Bulletin*, v. 124, no. 9-10, p. 1557-1561.

- Holliday, V.T. (1989). The Blackwater Draw Formation (Quaternary): A 1.4-plus-m.y. record of eolian sedimentation and soil formation on the Southern High Plains: *GSA Bulletin*, 101, 1598-1607.
- Holliday, V.T. (1995). Stratigraphy and Paleoenvironments of Late Quaternary Valley Fills on the Southern High Plains: *GSA Memoir*, 186.
- Holliday, V.T., Rawling, J.E. (2006). Soil-geomorphic relations of lamellae in eolian sand on the High Plains of Texas and New Mexico: *Geoderma*, 131(1-2), 154-180.
- Hovorka, S.D. (1997). Quaternary evolution of ephemeral playa lakes on the Southern High Plains of Texas, USA: cyclic variation in lake level recorded in sediments: *Journal of Paleolimnology*, 17, 131-146.
- Honisch, B., Hemming, N. G., Archer, D., Siddall, M., McManus, J. F. (2009). Atmospheric Carbon Dioxide Concentration Across the Mid-Pleistocene Transition: *Science*, 324(5934), 1551-1554.
- Jain, M., Botter-Jensen, L., & Singhvi, A. K., 2003. Dose evaluation using multiple-aliquot quartz OSL: test of methods and a new protocol for improved accuracy and precision. *Rad. Measur.* 37, 67-80.
- Jacobs, Z. (2010). An OSL chronology for the sedimentary deposits from Pinnacle Point Cave 13B-A punctuated presence: *Journal of Human Evolution*, 59(3-4), 289-305.
- Jacobs, Z., Roberts, R. G., Lachlan, T. J., Karkanas, P., Marean, C. W., Roberts, D. L. (2011). Development of the SAR TT-OSL procedure for dating Middle Pleistocene dune and shallow marine deposits along the Southern Cape coast of South Africa: *Quat. Geochronol.*, 6(5), 491-513.
- Kocurek, G., Lancaster, N. (1999). Aeolian system sediment state: theory and Mojave Desert Kelso dune field example: *Sedimentology*, 46, 505-515
- Lian, O. B., Hu, J. S., Huntley, D. J., and Hicock, S. R., 1995, Optical Dating Studies of Quaternary Organic-Rich Sediments from Southwestern British-Columbia and Northwestern Washington-State: *Canadian Journal of Earth Sciences*, v. 32, no. 8, p. 1194-1207.
- Liang, P., Forman, S.L., 2020. LDAC: An Excel-based program for luminescence equivalent dose and burial age calculations. *Ancient TL* 37 (2), 21-40.
- Lian, O.B., Hu, J.S., Huntley, D.J., Hicock, S.R. (1995). Optical dating studies of quaternary organic-rich sediments from Southwestern British-Columbia and Northwestern Washington-state: *Canadian Journal of Earth Sciences*, 32(8), 1194-1207.
- Lisiecki, L.E., Raymo, M.E. (2006). Plio-Pleistocene climate evolution: trends and transitions in glacial cycle dynamics: *Quat. Sci. Revs*, 26, 56-69.

- Mangan, J. M., Overpeck, J. T., Webb, R. S., Wessman, C., and Goetz, A. F. H., 2004, Response of Nebraska Sand Hills natural vegetation to drought, fire, grazing, and plant functional type shifts as simulated by the century model: *Climatic Change*, v. 63, no. 1-2, p. 49-90.
- McGee, D. (2020). Glacial-Interglacial Precipitation Changes: *Annu. Rev. Mar. Sci.*, 12, 525-557
- McKean, R.L.S., Goble, R.J., Mason, J.B., Swinehart, J.B., Loope, D.B. (2015). Temporal and spatial variability in dune reactivation across the Nebraska Sand Hills, USA: *Holocene*, 25(3), 523-535.
- Mejdahl, V. & Christiansen, H.H., 1994. Procedures used for luminescence dating of sediments. *Boreas* 13, 403-406.
- Menking, K. M., Polyak, V. J., Anderson, R. Y., and Asmerom, Y., 2018, Climate history of the southwestern United States based on Estancia Basin hydrologic variability from 69 to 10 ka: *Quaternary Science Reviews*, v. 200, p. 237-252.
- Muhs, D.R., Holliday, V.T. (2001). Origin of late quaternary dune fields on the Southern High Plains of Texas and New Mexico. *GSA Bulletin*, 113(1), 75-87.
- Muhs, D.R., Reynolds, R.L., Been, J., Skipp, G. (2003). Eolian sand transport pathways in the southwestern United States: Importance of the Colorado River and local sources: *Quat. Int.*, 104, 3-18.
- Murray, A.S. (1996). Developments in optically stimulated luminescence and photo-transferred thermoluminescence dating of young sediments, application to a 2,000-year sequence of flood deposits: *Geochim. Cosmochim. Acta.*, 60, 565-576
- Murray, A.S., Wintle, A.G. (2000). Luminescence dating of quartz using an improved single-aliquot regenerative-dose protocol: *Radiat. Meas.*, 32(1), 57-73.
- Murray, A.S., Wintle, A.G. (2003). The single aliquot regenerative dose protocol: Potential for improvements in reliability: *Radiat. Meas.*, 37(4-5), 377-381.
- Nelson, D.T., Jewell P.W. (2015). Transgressive stratigraphic record and possible oscillations of late Pleistocene Lake Bonneville, Northern Hogup Mountains, Utah, USA: *Palaeogeogr. Palaeoclimatol. Palaeoecol.*, 432, 58-67.
- Oviatt, C.G., Madsen, D.B., Schmitt, D.N. (2003). Late Pleistocene and early Holocene rivers and wetlands in the Bonneville basin of western North America: *Quat. Res.*, 60(2), 200-210.
- Patrickson, S.J., Sack, D., Brunelle, A.R., Moser, K.A. (2010). Late Pleistocene to early Holocene lake level and paleoclimate Insights from Stansbury Island, Bonneville Basin, Utah: *Quat. Res.*, 73(2), 237-246.
- Peng, L. & Forman, S. L., 2019. LDAC: An Excel-based program for luminescence equivalent dose and burial age calculations. *Ancient TL*.

- Porat, N., Duller, G.A.T., Roberts, H.M., Wintle, A.G. (2009). A simplified SAR protocol for TT-OSL: *Radiat. Meas.*, 44(5-6), 538-542.
- Prescott, J. R., and Hutton, J. T., 1994, Cosmic-Ray Contributions to Dose-Rates for Luminescence and Esr Dating - Large Depths and Long-Term Time Variations: *Radiation Measurements*, v. 23, no. 2-3, p. 497-500.
- Rawle, A., 2003. Basic principles of particle size analysis. *Surface Coatings International*, 86(2), 58– 65
- Reheis, M.C., Goodmacher, J.C., Harden, J.W., McFadden, L.D., Rockwell, T.K., Shroba, R.R., Sowers, J.M., Taylor, E.M., Quaternary soils and dust deposition in southern Nevada and California: *GSA Bulletin*, 107(9), 1003-1022.
- Rich, J. (2013). A 250,000-year record of lunette dune accumulation on the Southern High Plains, USA and implications for past climates: *Quat. Sci. Revs*, 62, 1-20.
- Rich, J., Stokes, S. (2011). A 200,000-year record of late Quaternary Eolian sedimentation on the Southern High Plains and nearby Pecos River Valley, USA: *Eolian Research*, 2(4), 221-240.
- Ruddiman, W.F., Raymo, M.E., Lamb, H.H., Andrews, J.T. (1988). Northern Hemisphere Climate Regimes During the Past 3 Ma: Possible Tectonic Connections [and Discussion]: *Philosophical Transactions of the Royal Society of London*, 318(1191), 411-430
- Saibi, H., 2017. Microgravity and Its Applications in Geosciences in *Gravity Geoscience Applications, Industrial Technology and Quantum Aspect* (ed. Zouaghi, T.) DOI: 10.5772/intechopen.71223.
- Schlesinger, W. H. (1990). "Greenhouse Warming - Vegetation an Unlikely Answer." *Nature* 348(6303): 679-679.
- Schmidt, M.W., Hertzberg, J.E. (2011). Abrupt Climate Change During the Last Ice Age. *Nature Education Knowledge* 3(10), 11
- Stevens, T., Buylaert, J.P., Murray, A.S. (2009). Towards development of a broadly applicable SAR TT-OSL dating protocol for quartz: *Radiat. Meas.*, 44(5-6), 639-645.
- Stokes, S., Thomas, D.S.G., Washington, R. (1997). Multiple episodes of aridity in southern Africa since the last interglacial period: *Nature*, 388, 154-158
- Tew-Todd, V., Forman, S.L. (2020). Late Quaternary stratigraphy and chronology by thermal-transfer optically stimulated luminescence dating of quartz grains for the Monahans eolian system, Winkler County, Texas. Masters Thesis (Baylor University, 2020).
- Trenberth, K. E. and J. W. Hurrell (1994). "Decadal Atmosphere-Ocean Variations in the Pacific." *Climate Dynamics* 9(6): 303-319.

- Tripaldi, A., Forman, S.L. (2016). Eolian depositional phases during the past 50 ka and inferred climate variability for the Pampean Sand Sea, western Pampas, Argentina: *Quat. Sci. Revs.* 139, 77-93.
- United States. Natural Resources Conservation Service., 2014. Keys to soil taxonomy. Washington, D.C., United States Department of Agriculture, Natural Resources Conservation Service.
- Wang, X.L., Wintle, A.G., Lu, Y.C. (2007). Testing a single-aliquot protocol for recuperated OSL dating: *Radiat. Meas.*, 42(3), 380-391.
- Wentworth, C. K., 1922. "A scale of grade and class terms for clastic sediments." *Journal of Geology* 30(5): 377-392. Wintle, A.G., & Murray, A.S., 2006. A review of quartz optically stimulated luminescence characteristics and their relevance in single-aliquot regeneration dating protocols. *Rad. Measur.* 41, 369-391.
- Wintle, A.G., Murray, A.S. (2006). A review of quartz optically stimulated luminescence characteristics and their relevance in single-aliquot regeneration dating protocols. *Radiat. Meas.*, 41, 369–391
- Yann, L.T., DeSantis, L.R.G., Haupt, R.J., Romer, J.L., Corapi, S.E., Ettenson, D.J. (2013). The application of an oxygen isotope aridity index to terrestrial paleoenvironmental reconstructions in Pleistocene North America: *Paleobiology*, 39(4), 576-590.